

Regional impacts of iron-light colimitation in a global biogeochemical model

Eric D. Galbraith^{1*}, Anand Gnanadesikan², John P. Dunne², Michael R. Hiscock¹

[1]{ AOS Program, Princeton University, Princeton, NJ 08544}

[2]{ NOAA Geophysical Fluid Dynamics Laboratory, Princeton, NJ 08542}

[*]{now at: Department of Earth and Planetary Science, McGill University, Montreal, QC}

Correspondence to: E. D. Galbraith (eric.galbraith@mcgill.ca)

Abstract

Laboratory and field studies have revealed that iron has multiple roles in phytoplankton physiology, with particular importance for light-harvesting cellular machinery. However, although iron-limitation is explicitly included in numerous biogeochemical/ecosystem models, its implementation varies, and its effect on the efficiency of light harvesting is often ignored. Given the complexity of the ocean environment, it is difficult to predict the consequences of applying different iron limitation schemes. Here we explore the interaction of iron and nutrient cycles using a new, streamlined model of ocean biogeochemistry. Building on previously published parameterizations of photoadaptation and export production, the Biogeochemistry with Light Iron Nutrients and Gasses (BLING) model is constructed with only three explicit tracers but including macronutrient and micronutrient limitation, light limitation, and an implicit treatment of community structure. The structural simplicity of this computationally inexpensive model allows us to clearly isolate the global effects of iron availability on maximum light-saturated photosynthesis rates from those of photosynthetic efficiency. We find that the effect on light-saturated photosynthesis rates is dominant, negating the importance of photosynthetic efficiency in most regions, especially the cold waters of the Southern Ocean. The primary exceptions to this occur in iron-rich regions of the northern hemisphere, where high light-saturated photosynthesis rates cause photosynthetic efficiency to play a more important role. Additionally, we speculate that the small phytoplankton dominating iron-limited regions tend to have relatively high photosynthetic efficiency, such that iron-limitation has less of a deleterious effect on growth rates than would be expected from short-term iron addition experiments.

1 Introduction

In large surface regions of the open ocean, macronutrients remain in considerable abundance throughout the year, a puzzle that has engaged the interest of oceanographers for many decades. These regions contrast with coastal environments in which the surface ecosystem handily strips out macronutrients, despite high resupply rates. Although many factors have been implicated in the maintenance of the nutrient-rich surface oceans, limitation by micronutrients – principally iron – clearly plays a central role.

Over the past decades, numerous experiments have shown that adding iron to macronutrient-rich regions of the ocean produces plankton blooms (see Boyd et al. 2007 for a review). On a physiological level, this appears to be largely due to the role of iron in the electron transport pathways that accomplish photosynthesis (Raven, 1990; Maldonado et al., 1999); cells that are replete in iron can build more photosynthetic reaction centers and utilize the light they collect more efficiently (Greene et al., 1991; Strzepek and Harrison, 2004). Iron is also required for other cellular processes, including the reduction of nitrate to ammonia (Raven, 1990; Price et al., 1991). Laboratory studies support this, reporting large decreases in growth rates under iron limitation (Price et al., 1991; Greene et al., 1991; Sunda and Huntsman, 1995; Timmermans et al., 2004). In addition, iron deficiency has been shown to significantly reduce the chlorophyll to carbon ratio, θ , in almost all cases, due to the requirement for iron in chlorophyll biosynthesis (e.g. Greene et al., 1991; Sunda and Huntsman, 1995; Marchetti et al., 2007).

While the impact of iron on photosynthesis is clearly important, the manner in which its effects should be implemented in numerical models is less clear. Recent representations of algal physiology in biogeochemical models have often relied on the photoadaptation scheme of Geider et al. (1997), used in numerous global models (e.g. Moore and Doney, 2002; Aumont and Bopp, 2006). This scheme is built around a common expression for the carbon-specific photosynthesis rate, P^C , as a function of irradiance, I ,

$$P^C = P_m^C \{1 - \exp(-I/I_k)\} \quad (1)$$

where P_m^C is a macronutrient-limited, temperature-dependent, light-saturated carbon-specific photosynthesis rate (s^{-1}) and I_k is a scaling term that determines the degree of light-limitation (W m^{-2}). Note that photosynthesis is always light limited to some degree in this formulation (since $\{1 - \exp(-I/I_k)\}$ is always less than 1), and that for a given I , photosynthesis decreases

with increasing I_k . In the model of Geider et al. (1997), θ adapts to a phytoplankter's nutritional status, temperature, and light environment in a way that is consistent with laboratory experiments. This leads to a formulation for I_k as a function of P_m^C , θ , and α^{chl} , the latter of which is the initial slope of the chlorophyll-*a* specific photosynthesis-light response curve (units of g C g chl⁻¹ W⁻¹ m² s⁻¹). This latter term governs how rapidly photosynthesis (relative to chlorophyll) increases with increasing light at low light levels, essentially a metric for the yield of usable photons harvested by each molecule of chlorophyll under low light (Frenette et al., 1993; Hancke et al., 2008). Substituting the Geider et al. (1997) formulation for θ in their equation for I_k , we rearrange to obtain

$$I_k = \frac{P_m^C}{\alpha^{chl} \theta_{\max}} + \frac{I_{mem}}{2} \quad (2)$$

where θ_{\max} is a maximum chlorophyll-to-carbon ratio (g chl gC⁻¹) and I_{mem} is the irradiance to which the phytoplankton are accustomed. This equation captures the capacity of phytoplankton to adjust their photosynthetic machinery to their environment, in order to maximize photosynthesis rates while minimizing metabolic costs.

Within this widely-applied conceptual framework, the experimental evidence suggests that iron limitation could impact the growth of phytoplankton in three obvious ways. First, it could reduce the light-saturated growth rate P_m^C . This would represent the need for iron in proteins that mediate photosynthetic electron transport (Raven, 1990) and thereby determine the maximum yield of electrons for photosynthesis when light is abundant. Additionally, this term accounts for the utility of iron for non-photosynthetic processes such as nitrate reduction (Price et al., 1991). However, if P_m^C is the only iron-dependent term, low iron will have the effect of making the plankton less light-limited, as they will need less light to match the other cellular functions (see the first term of eq. 2). In other words, because Fe limitation reduces the maximum achievable photosynthetic rate, the utility of photons would decrease under Fe limitation, making light availability less important. This tendency would be counteracted by including iron dependencies in the two other obvious terms: α^{chl} , so that photosynthetic efficiency decreases at low light under iron limitation, representing a reduction of the reaction centers available for light harvesting elements; and θ_{\max} , so that iron deficiency reduces chlorophyll synthesis and thereby cause θ_{\max} to decrease. Note that the second and third

mechanisms are numerically linked in the photosynthesis formulation, through modification of I_k as the product $1/\alpha^{chl}\theta_{\max}$.

Applying iron dependencies to these three terms appears to broadly reflect the available measurements of photosynthetic parameters made during bottle incubations and mesoscale iron fertilization experiments. For example, in bottle incubations of natural samples from the Drake Passage, Hopkinson et al. (2007) reported that iron addition increased α^{chl} , θ and P_m^B (the light-saturated chlorophyll-specific growth rate, equal to P_m^C/θ). Marchetti et al. (2006) also reported large increases in these three parameters, within an iron-fertilized patch of the subarctic Pacific during the SERIES experiment. Hiscock et al. (2008) presented observations from the SOFeX mesoscale iron enrichment experiment, showing an increase of α^{chl} by about 70% while quantum yield (effectively $\alpha^{chl}\theta$) increased by about twice as much, a factor of ~ 2.5 . However, in their case the chlorophyll-specific photosynthesis rate P_m^B remained relatively unchanged, indicating that any change in P_m^C was approximately balanced by a corresponding change in θ . Taken together, these results suggest that P_m^C , θ and α^{chl} can all change significantly as a function of Fe availability, although the magnitudes of the changes vary. However, many biogeochemical models only include the effect of iron on P_m^C , while variation in θ and α^{chl} may arise indirectly, through changes in plankton composition (for models in which plankton functional types have different photosynthetic parameters), or not at all. Hence, it is useful to understand how including an iron dependency for each of these three photosynthetic parameters affects global biogeochemical cycling.

Although including additional iron limitation terms within the photosynthesis formulation is relatively straightforward, understanding their net impact on a global model is not. Introducing iron limitation alters the spatiotemporal distribution of nutrients, chlorophyll, and biomass in a way that will depend on the representation of grazing and export, the physical circulation regime, and the iron cycle itself. Understanding the dynamics of iron limitation at the global scale requires global models that consider both realistic physical transport and biology, and which can be deliberately manipulated in order to target isolated components of the problem. However, comprehensive state-of-the-art biogeochemical schemes used in earth system modeling typically include multiple functional groups with differing responses to iron and nutrient limitation, complex zooplankton dynamics (Aumont et al., 2003), interactions between nitrogen fixation and iron limitation (Doney et al., 2007, Moore et al. 2007), and

interactions between the global oxygen cycle and nutrient limitation via denitrification (Schmittner et al., 2006), all of which introduce complicating feedbacks.

This paper presents a new model of global biogeochemical cycling (Biogeochemistry-with-Light-Iron-Nutrients-Gas or BLING) that includes a physiologically-based representation of light limitation and explicitly simulates limitation by both iron and a macronutrient, but parameterizes the net effects of community size structure, grazing, and export following the work of Dunne et al. (2005). Thus, it presents a reasonable framework in which to isolate the physiological effects of iron limitation, without nonlinear interactions between ecosystem components and other elemental cycles. The model is described in detail in Section 2. We then describe a series of experiments in which we isolate the impacts of iron dependencies on the global biogeochemical simulation, as described in Sections 3. Section 4 concludes the paper.

2 Model description

BLING was developed as an intermediary between complex, highly nonlinear biogeochemical-ecosystem models (e.g. Moore et al., 2004; Aumont and Bopp, 2006) and simple, idealized biogeochemical models, that either ignore representation of ecosystem dynamics (e.g. Dutkiewicz et al., 2005; Doney et al., 2006) or that generate export production by forcing surface nutrients towards observations (e.g. Najjar and Orr, 1999; Gnanadesikan et al., 2002, 2004). Like these other coupled ocean-biogeochemical models, BLING is designed to be embedded within an ocean general circulation model, and produces a three dimensional solution that changes with time according to the physical ocean environment.

BLING uses a relatively complex growth and export formulation, and is fully prognostic, in that the output depends only on in situ parameters provided by a physical circulation model, without restoring to observations. It is also ‘continuous’, in that all equations are solved in all grid cells, with no arbitrary division between a shallow interval of export production and a remineralizing deep ocean; this allows ocean metabolism to arise purely from the physical forcing. Despite these features, the model only requires three explicit tracers, which we call dissolved inorganic phosphorus (PO_4), dissolved organic phosphorus (DOP) and dissolved iron (Fe). It achieves this by treating the ecosystem implicitly, i.e. without any tracers that explicitly represent organisms. The core behavior of the model can therefore be thought of as an ‘NPZD’ (nutrient, phytoplankton, zooplankton and detritus) model where the P, Z and D

tracers are treated implicitly, so that computationally it is simply an ‘N’ model. As discussed below, the remineralization is dependent on the oxygen concentration. For this reason, as well as to better understand impacts of changes in productivity, we also carry an oxygen (O₂) tracer for a total of four prognostic tracers (Figure 1). As a result, BLING is suitable for use in well-resolved physical models that include mixed-layer dynamics and a diurnal cycle, while remaining less complex and less computationally intensive than full ecosystem models.

Here we describe the version of the model used for the experiments in this paper, referred to as BLING.v0. Further information, updates, and model code will be made available on the website <http://sites.google.com/site/blingmodel/>.

2.1 Growth rate formulation

The growth rate of phytoplankton (μ) is calculated as a function of the ambient water characteristics: nutrient concentrations, light, and temperature. While the macronutrient- and temperature-dependent formulations used here are very typical of biogeochemical-ecosystem models, we use a novel scheme for representing iron limitation that does not rely exclusively on Liebig’s law of the minimum (by which only the most limiting nutrient affects growth) but also incorporates nutrient-light co-limitation in a way that is broadly consistent with laboratory and field studies of phytoplankton.

The growth rate calculation begins by determining the light-saturated photosynthesis rate from the *in situ* conditions,

$$P_m^C = P_0^C \times \exp(kT) \times \min\left(Def_{fe}, \frac{PO_4}{K_{PO_4} + PO_4}\right) \quad (3)$$

which depends on a specified maximum photosynthesis rate at temperature T=0°C (P_0^C), a temperature-dependent term with $k=0.063 \text{ } ^\circ\text{C}^{-1}$ following Eppley (1972), and a limitation by iron and phosphate following Liebig’s law of the minimum. Phosphate limitation is given by the simple Monod relationship as shown, which depends only on the half-saturation constant K_{PO_4} , while Fe limitation is expressed by the term Def_{fe} as described below.

In calculating Def_{fe} we represent the fact that, in contrast to nitrogen and carbon, Fe is taken up by phytoplankton in a highly variable ratio to phosphorus (e.g. Sunda & Huntsman, 1997,

Marchetti et al., 2006b, Boyd et al., 2007). We calculate this uptake ratio directly from the ambient water chemistry as

$$(Fe:P)_{uptake} = (Fe:P)_0 * \frac{Fe}{K_{fe} + Fe} \quad (4)$$

where Fe is the dissolved iron concentration, $(Fe:P)_0$ is a maximal uptake ratio and K_{fe} defines the half-saturation constant for the uptake ratio. Although very simple, this formulation results in a correlation between $(Fe:P)_{uptake}$ and dissolved Fe concentrations that approximates the response shown in laboratory studies such as that of Sunda and Huntsman (1997). Since, for balanced growth, the uptake ratio is equal to the cell quota, we can calculate iron limitation directly from $(Fe:P)_{uptake}$,

$$Def_{Fe} = \frac{(Fe:P)_{uptake}}{K_{Fe:P} + (Fe:P)_{uptake}} \times \frac{K_{Fe:P} + (Fe:P)_0}{(Fe:P)_0} \quad (5)$$

where $K_{Fe:P}$ defines the half-saturation cellular Fe:P quota, i.e. the ratio at which the iron limitation term equals 0.5. The second term in equation 5 normalizes the expression, so that at high concentrations of dissolved iron, Def_{Fe} approaches 1. Treating uptake in this fashion allows the implicit cellular Fe:P to increase as Fe concentrations increase, but with diminishing physiological returns, consistent with the notion of ‘luxury’ uptake (Sunda and Huntsman, 1995; Marchetti et al., 2009).

Iron limitation can also be applied to two additional components of the general Geider et al. (1997) photosynthesis rate formulation, introduced in eq. 2 above, as follows:

$$\alpha^{chl} = \alpha_{min}^{chl} + (\alpha_{max}^{chl} - \alpha_{min}^{chl}) \times Def_{Fe} \quad (6a)$$

$$\theta_{max}^{Fe} = \theta_{min} + (\theta_{max} - \theta_{min}) \times Def_{Fe} \quad (6b)$$

where θ_{max}^{Fe} modulates θ by replacing θ_{max} . Together, these exacerbate the tendency for light limitation under iron stress, representing co-limitation by iron and light. Note that we chose linear dependencies in order to minimize complexity, rather than based on first principles. The overall, light-limited photosynthesis rate is then calculated by equation (1), in which I is the in-situ irradiance, except within the mixed layer where the irradiance is vertically averaged in order to implicitly represent the turbulent transport of phytoplankton throughout the mixed layer. Note that the irradiance used for calculating θ and $I_k(I_{mem})$ is smoothed over one day to represent a small lag as phytoplankton adapt to ambient light levels (Dusenberry et al., 2001).

Even with this small number of equations, the resulting interdependence on iron, light, temperature, and macronutrient is significantly nonlinear. As illustrated in Figure 2, the Geider (1997) formulation predicts that the total photosynthesis rate P^C increases as I increases, but the response to I saturates more quickly when P_m^C is small (either because of nutrient limitation or low temperature), since fewer photons are required to achieve the slower light-saturated photosynthesis rates. This can be seen by inspection of equation 2, in which the first term, $P_m^C / \alpha^{chl} \theta_{\max}^{Fe}$, gives the dependence of light limitation on temperature and nutrient availability: when this term is large, more light is required to approach light-saturated rates. Equation 2 also reveals that the iron dependencies of α^{chl} and θ_{\max}^{Fe} carry more weight when P_m^C is large, and/or when the second term of equation 2 ($I/2$) is small. Thus, under low light, and at high temperatures, iron limitation has a larger impact on the degree of light limitation. Meanwhile, at high PO_4 concentrations, Fe has a very large impact on P_m^C through the Liebig limitation term, whereas when PO_4 concentrations limit P_m^C , iron limitation mainly acts through its effect on I_k .

Finally, combining our iron limitation scheme with the Geider et al. (1997) formulation, we can diagnose a chlorophyll to carbon ratio

$$\theta = \frac{\theta_{\max}^{Fe}}{1 + \alpha^{chl} \theta_{\max}^{Fe} I_{mem} / 2P_m^C} \quad (7)$$

Increasing the iron concentration will thus affect θ via all three iron-dependent terms. First, the increase of P_m^C will increase θ , as plankton manufacture chlorophyll in an attempt to provide energy to achieve the higher light-saturated photosynthesis rate. Second, the increase of θ_{\max}^{Fe} will cause θ to increase, with more impact at low light levels than at high light levels. Third, an increase of α^{chl} will tend to *decrease* θ , particularly at high light (since a given amount of chlorophyll becomes more efficient at processing light). The net effect of iron addition on θ , as well as growth rate, is therefore dependent on multiple environmental conditions.

The carbon-specific growth rate, μ , is equal to the photosynthesis rate minus respiration. For simplicity, we follow Geider et al. (1997) in assuming that respiration is a fixed fraction of the growth rate, and is thus incorporated into P^C for the experiments described here, so that $\mu = P^C$ for the remainder of the discussion. All calculations are made in terms of phosphorus,

and are converted to carbon units assuming a constant C:P of 106 and to oxygen units using an O₂:P of 150 (Anderson, 1995).

2.2 Mortality rate formulation

The uptake of nutrients by phytoplankton depends on the carbon-specific growth rate, multiplied by the biomass of living phytoplankton. The biomass, in turn, evolves due to a small residual between total growth and total mortality rates. Many models keep track of these terms explicitly, allowing direct calculation of mortality, but incorporating additional computational expense. However, it is also possible to calculate the biomass associated with a particular growth rate implicitly, circumventing the need for explicit biomass tracers, if we apply a simple mortality law.

Following the global observational synthesis of Dunne et al. (2005) we assume a mortality law of the form

$$Growth = \mu B = \lambda_T (B/P^*)^a B = Mortality \quad (8)$$

where B is the biomass in mol P kg⁻¹, λ_T is the temperature-dependent mortality rate (equivalent to the sum of all losses of living biomass through grazing, viral lysis, etc.) and P^* is a scaling term. The term a represents a mortality exponent, as discussed by Dunne et al. (2005). If $a=1$, the formulation corresponds to classic logistic growth, in which the mortality rate is linearly proportional to population density. If we assume that the temperature dependence of mortality is identical to that of growth such that $\lambda_T = \lambda e^{kT}$, the biomass B_x associated with the growth rate of a particular class of phytoplankton x is $B_x = (\mu_x / \lambda e^{kT})^{1/a_x} \times P^*$ so that the uptake rate of PO₄ is given as

$$V_{PO_4_x} = (\mu_x / \lambda e^{kT})^{1/a_x} \times P^* \times \mu_x \quad (9)$$

Following most ecosystem models, we conceptualize the phytoplankton as including two subpopulations: ‘large’, which are consumed by mesozooplankton and are more likely to form more sinking particles, and ‘small’, which are consumed by microzooplankton and are more likely to decompose to dissolved and suspended organic matter. If we assume that small and large phytoplankton growth rates are the same under the same conditions (probably incorrect, but a useful simplifying assumption), $B_x = (\mu / \lambda e^{kT})^{1/a_x} \times P^*$. We follow Dunne et al. (2005)

in using $a = 1$ for small phytoplankton (corresponding to an assumption that the rapidly reproducing microzooplankton concentrations match small phytoplankton concentrations) and $a = 1/3$ for large phytoplankton.

This formulation produces a cubic relationship between large and small plankton, consistent with the field data compilation of Agawin et al. (2000), and represents a fundamental building block both of our model and of the more complex TOPAZ biogeochemical model (Dunne et al., in prep.), used in the GFDL Earth System Model. The total uptake is then

$$V_{PO_4} = ((\mu/\lambda e^{kT})^3 + (\mu/\lambda e^{kT})) \times \mu \times P^* \quad (10)$$

Following Dunne et al. (2005) we use values of $\lambda=0.19 \text{ day}^{-1} e^{kT}$ and $P^*=1.9 \mu\text{mol C kg}^{-1}$.

This key relationship allows us to diagnose a number of useful properties. For example, the biomass is

$$B = ((\mu/\lambda e^{kT})^3 + (\mu/\lambda e^{kT}))P^* = B_{large} + B_{small} \quad (11)$$

Note that since the temperature dependence e^{kT} appears in both the numerator and denominator of each term, the biomass itself is independent of temperature. From (9) the fraction of biomass associated with large phytoplankton $frac_L$ is simply

$$frac_L = \frac{B_{large}}{B_{large} + B_{small}} = \frac{(\mu/\lambda e^{kT})^2}{1 + (\mu/\lambda e^{kT})^2} \quad (12)$$

such that at 0°C , if the growth rates exceed $\sim 0.19 \text{ day}^{-1}$, large phytoplankton will be in the majority, while at 28°C the growth rate must exceed 1.1 day^{-1} for this to be true.

2.3 Organic matter cycling

Field observations show that nutrient elements are efficiently recycled within the mixed layer, with a relatively small fraction being exported as dissolved or particulate organic material (Dugdale and Goering, 1967). In order to model a realistic relationship between gross primary production and export production, we must therefore represent the division of nutrient uptake between recycling and export. Once again we follow the work of Dunne et al. (2005) who examined 119 globally distributed sites at which the ratio between particulate export and primary production (the pe-ratio) could be estimated from observations. They developed a formulation that linked the pe-ratio to water column remineralization, in terms of the

production of detritus and ballasting material associated with coccolithophorids and diatoms. As we do not explicitly represent sinking detritus, we reanalyze the Dunne et al. (2005) dataset in terms of a simpler model of particle sinking and remineralization.

As was recently noted by (Kriest and Oschlies, 2008) the classic “Martin curve” profile for remineralization is consistent with a sinking speed that increases linearly with depth and a remineralization rate that is constant. We chose a sinking speed of 16 m/day over the top 80m, increasing linearly below that depth at a rate of 0.05(m/day)/m and an oxygen-dependent remineralization rate with a maximum of γ_{DOP} of 0.12 day⁻¹. Figure 3a shows the resulting profile of particle flux, which lies between the classic Martin curve of $F = F(z = 100m) \times (z/100)^{-0.868}$ and the function $F = F(z = 75m) \times (z/75)^{-0.9}$ used for the OCMIP2 simulations (see for example Gnanadesikan et al., 2002, 2004). The remineralization rates (% primary production/m), shown in Figure 3b, are similar to the previous parameterizations over most of the water column.

Following Dunne et al. (2005) we link large and small phytoplankton to a remineralization scheme to derive a particle export ratio. We calculate values of ϕ_L and ϕ_S , the detrital production fractions associated with large and small phytoplankton respectively, to match the observational compilation in Dunne et al. (2005). The resulting values of $\phi_L = 1.0$ and $\phi_S = 0.18$ provide a fit that explains more than 60% of the variance in the observations, as illustrated in Figure 3c, comparable to the fits found in Dunne et al. (2005). The detritus production tends to be less than half the total uptake, and can be as little as one tenth in warm, low-productivity waters. The non-detritus remainder is then subdivided, such that a constant fraction ϕ_{DOP} is converted to dissolved organic phosphorus, with the residual being instantaneously recycled to inorganic PO₄ to represent the microbial loop (Figure 1). The magnitude of gross uptake (primary production) is strongly dependent on this subdivision, but it has little effect on export production. The remineralization of sinking detritus also produces both dissolved inorganic and dissolved organic phosphorus, in the same ratio ϕ_{DOP} .

2.4 Iron cycling

The iron cycle is inherently more complex than the phosphate cycle, primarily because dissolved iron concentrations are more intensely modified by interactions with particles than

are dissolved phosphate concentrations (Parekh and Boyle, 2005). In an oxygenated environment, iron (II) and (III) form colloids that are readily scavenged by organic and mineral sinking particles, removing them from the water column (Wu et al., 2001). On the other hand, iron can also be chelated by dissolved organic ligands, whose concentrations can greatly exceed that of the iron itself, preventing the adsorption of iron to particles (Rue and Bruland, 1995). Meanwhile, the uptake of chelated iron by plankton (Tortell et al., 1999) and the photochemical breakdown of ligands (Barbeau et al., 2001) can result in relatively short lifetimes for iron in the surface ocean (Weber et al., 2005; Tagliabue and Arrigo, 2005). As a result of its high reactivity and rapid removal from the ocean, the lifetime of iron in the ocean is much shorter than that of phosphate or nitrate, resulting in a tight coupling of the iron distribution to its source regions (Johnson et al., 1997). These sources include runoff (Hutchins et al., 1998), mineral dust (Mahowald et al., 2003; Ginoux et al. 2004) and sediments (Lam et al., 2006; Moore and Braucher, 2008).

Given that the understanding of multiple forms of iron remains rudimentary, we follow previous workers (e.g. Moore et al., 2004; Parekh et al., 2004; Aumont and Bopp, 2006) in defining a single pool of ‘dissolved’ iron. Iron is supplied to the ocean surface layer according to a prescribed climatological aeolian dust source (Ginoux et al., 2004) which totals 3.28 Gmol Fe a⁻¹. Iron is also supplied by diffusion from the seafloor, representing the release of iron from organic and mineral phases in the sediment, as the product of $Fe:P_{sed}$ and the sedimenting organic phosphorus flux, following Moore and Braucher (2008). The sedimentary iron efflux varies with global export production, but is on the order of 8 Gmol Fe a⁻¹.

We also include an implicit ligand, with a globally uniform concentration of 1 nM following Parekh et al. (2005). We allow the ligand stability constant K_{FeL} to decrease from K_{FeL}^{max} toward K_{FeL}^{min} in surface waters, which are diagnosed as a function of light intensity I , inspired by the observed photodissociation of iron-ligand complexes in surface waters (Barbeau et al., 2001, 2003):

$$K_{FeL} = K_{FeL}^{max} - (K_{FeL}^{max} - K_{FeL}^{min}) * \frac{I^2}{I_{FeL}^2 + I^2} * \max(0, \min(1, \frac{Fe - Fe_{min}}{Fe} * b)) \quad (13)$$

where b is an arbitrary multiplier (equal to 1.2) to ensure that K_{FeL} approaches K_{FeL}^{max} . Since ligands and their reaction to light are not explicitly modeled, the light sensitivity parameter,

I_{FeL} , is set to a low value to maintain low values of K_{FeL} throughout the euphotic zone. The latter term in eq. 13 reduces photodissociation when iron concentrations Fe approach Fe_{min} , to represent the formation of siderophores (strong ligands) by microbes under iron stress (Trick et al. 1983, Granger and Price, 1999). This results in a more rapid removal of iron from the surface ocean, a result that Moore and Braucher (2008) achieve instead by increasing the scavenging rate constant by roughly a factor of 6 in the upper ocean.

Free dissolved iron, i.e. not bound to the ligand, is scavenged by two mechanisms in oxic waters. The first, after Parekh et al. (2005), calculates a first-order scavenging rate constant as a function of the sinking flux of organic matter:

$$Fe_{ads}^{org} = k_{Fe}^{org} * \left(\frac{f_{POC}}{w}\right)^{0.58} * Fe' \quad (14)$$

where the exponent of 0.58 is taken from the empirical study of Honeyman et al. (1988). Alone, this would ignore the unresolved effect of lithogenic material as a scavenging agent, as well as the inorganic formation of colloids. Therefore we include a second type of scavenging to represent these processes:

$$Fe_{ads}^{inorg} = k_{Fe}^{inorg} \times Fe'^{1.5} \quad (15)$$

Because the underlying processes are poorly understood, we use a globally uniform rate constant, and increase the order of the iron concentration dependence to represent the enhanced formation of colloids where iron concentrations are higher. Improving these parameterizations is a clear target for future work.

It is assumed that scavenged iron is released to the water column as it sinks; thus, adsorbed iron is returned to the dissolved pool following the same instantaneous sinking and remineralization routine applied to the particulate organic iron produced by phytoplankton uptake. Particulate iron that sinks out of the bottom ocean layer is permanently removed from the ocean, as long as oxygen concentrations are greater than the anoxic threshold. Otherwise, the sedimented iron is instantaneously returned to the bottom layer.

2.5 Parameter choices

Parameter values (shown in Table 1) were initially selected based on a survey of the available literature and/or first principles, and adjusted when necessary in order to obtain a solution that

compares reasonably well with observations. Note that the parameter ranges for α^{chl} and θ_{\max}^{Fe} were set to provide identical responses to Def_{Fe} , rather than as optimal fits to the data. The simulation was compared to the World Ocean Atlas 2001 and 2005, the dissolved iron compilation of Moore and Braucher (2008), the A16 section of Measures et al. (2008), and SeaWiFS satellite observations of chlorophyll (Level 3 SeaWiFS chlorophyll-a concentration data, OC4, reprocessing v5.2, for September 1997 - December 2007, downloaded from <http://oceancolor.gsfc.nasa.gov/>). Note that the sedimentary iron efflux ratio was reduced significantly from its initial value, in order to avoid overwhelming the relatively small atmospheric source.

2.6 Physical model

The BLING model was embedded in the ocean component of the GFDL coarse-resolution global coupled climate model, CM2Mc (Galbraith et al., in prep). This uses the MOM4p1 code with pressure as the vertical coordinate, a free surface, ‘real’ freshwater fluxes and a dynamic-thermodynamic sea ice module. The nominal resolution of this model, OM1p7, is 3 degrees in the east-west direction, with resolution in the north-south direction varying from 3 degrees in mid-latitudes to 2/3 degree near the equator. Enhanced resolution is also applied at the latitudes of the Drake Passage as well as at the symmetrically equivalent latitudes of the northern hemisphere. A tripolar grid is applied to the Arctic, as in GFDL’s CM2.0 and CM2.1 models (Griffies et al., 2005). The vertical resolution is 28 levels, ranging from 10 m resolution at the surface to 506 m in the lowermost layer. Tracer advection uses the Sweby MDFL scheme. The surface forcing is a repeated climatological year derived from the Coordinated Ocean Reference Experiment (Griffies et al., 2009), which also supplies shortwave irradiance to the ocean (there is no diurnal cycle). Surface salinities are restored to observations with a time constant of 10 days over the top layer. Light is absorbed by water and a smoothly-varying, satellite-derived climatological chlorophyll field following the Manizza et al. (2005) algorithm.

Subgridscale parameterizations for mixing are similar to those used in the CM2.1 series (Gnanadesikan et al., 2006). The lateral friction uses an isotropic Smagorinsky viscosity in mid-latitudes, while within 20 degrees of the equator the anisotropic NCAR viscosity is used, as in the CM2 series. Lateral diffusion of tracers along isopycnals is subject to the thickness

diffusion parameterization of Gent and McWilliams (1990) with a spatially varying diffusion coefficient. The time scale in this coefficient depends on the horizontal shear between 100m and 2000m while the spatial scale is constant. A minimum coefficient of 500 m²/s and a maximum coefficient of 1200 m²/s are imposed. The lateral diffusion coefficient for tracers is the same as the lateral diffusion coefficient for thickness. The thickness transport saturates at a value $A_I \cdot S_{\max}$ where S_{\max} is set to 0.02 (see Gnanadesikan et al., 2007 for discussion of potential impacts of this parameter). Within the mixed layer, we use the K-profile parameterization of Large et al., (1993). Away from the mixed layer, a background diffusivity of $0.1 \times 10^{-4} \text{ m}^2 \text{ s}^{-1}$ and a background viscosity of $1 \times 10^{-4} \text{ m}^2 \text{ s}^{-1}$ is used. Below 500m, these background coefficients are enhanced by using the scheme of Simmons et al. (2004) to parameterize a tidally-dependent mixing that depends on the in situ stratification as well as prescribed bottom roughness and tidal amplitude.

2.7 Model simulations

Because the performance of the biogeochemical model intimately depends on the physical model in which it is embedded, we refer to the coupled ocean-biogeochemical model here as BLING-om1p7. Initial conditions for ocean temperature and salinity were interpolated from the World Ocean Atlas 2001 to the model grid, and the model was started from rest. Phosphate and oxygen concentrations were taken from the World Ocean Atlas 2005. Iron was initialized from a constant global value of 0.6 nM and integrated for 200 years with a preliminary version of the model, to prevent large drift upon initialization. The model was then spun up for 400 years with the AllVar configuration (see below), allowing for the iron cycle and the nutrient structure of the thermocline to come to near equilibrium. Over the final century RMS changes in surface phosphate were less than 0.01 μM in this run, indicating that we have reached a relatively steady state at the surface. A suite of eight experiments was then initialized from this spun-up state, and each was integrated for 100 years. These form the basis of the discussion in part 3. In all cases, the final year of each run was analyzed.

We describe here the global simulation of the model experiment that includes all three iron limitation terms (which we refer to below as AllVar). The model simulates surface macronutrient concentrations with reasonable fidelity. Note that, although nitrogen is the more important limiting macronutrient in the ocean, we refer to our limiting macronutrient as

‘PO₄’, because we do not include denitrification and nitrogen fixation. We therefore compare our modeled PO₄ to an “average macronutrient” equal to (phosphate+nitrate/16)/2. The last column in Table 2 shows correlation and regression coefficients between the modeled macronutrient and the average macronutrient in this simulation. Correlation and regression coefficients all exceed 0.87, and the overall patterns of surface macronutrients are generally realistic (Figure 4a,b). The annual standard deviation of nutrient concentrations (Figure 4c,d) exhibits a large-scale similarity between modeled concentration and observations, with small ranges in the subtropical gyres and larger ranges along the equator, in the Southern Ocean and in northern subpolar gyres. The data (Figure 4d) has a lot of small-scale variability, much of which may result from undersampling and interpolation; in addition, when biases in the physical circulation are considered, the correlation of 0.58 is not unreasonable.

As seen in Figure 5, this experiment also reproduces the contrast between low-chlorophyll gyre centers and the higher chlorophyll upwelling zones and subpolar regions, as seen in satellite observations. The regression coefficient for the log chlorophyll concentration is 0.86, while the correlation coefficient is 0.90. The low value of the regression coefficient is likely related to the inability of BLING-om1p7 to reproduce intense blooms in coastal regions.

The simulated surface concentration of iron (Figure 6a) range from high values (exceeding 1.5 nM) in coastal regions, with relatively high values of 0.8-1.0 nM in the dust deposition plumes of the Atlantic and Northern Indian Oceans, similar to the data compilation of Moore and Braucher (2008). Significant seasonal cycles (Figure 6b) occur over much of the world ocean, with large variations beneath dust plumes, in convective regions and in the western parts of subtropical gyres. These seasonal cycles are due to resupply of iron during deep mixing, removal of iron by sinking particulate organic matter during the growth season, and the seasonal cycle of iron deposition, and likely contribute to small-scale variability in the observational database (Figure 6a). Measures et al. (2008) recently published a high-resolution section of iron along the A16N track. Figure 6c shows that the model produces a very similar spatial structure with low values in the surface North Atlantic and immediately south of the Equator, with higher values at depth and a plume of high iron north of the equator, centered around 15°N. Our values are somewhat lower than observed, particularly beneath the Saharan plume, but otherwise the agreement is encouraging given the many uncertainties in the source and sink terms for iron. The response of photosynthesis to spatial variations of dissolved iron is given by the term Def_{Fe} in the model, presented in equation (5).

As shown in Figure 6d, Def_{Fe} is near 1 (no limitation) close to shallow sediments, and near deserts where dust deposition is high. In the northern subpolar gyres it ranges between values of 0.4 and 0.6 while in the equatorial Pacific and Southern Ocean values of 0.1-0.3 are found. Iron limitation thus introduces spatial asymmetries between the hemispheres, as well as between the equatorial Atlantic and Pacific Oceans.

Following Gnanadesikan et al. (2004) and Dunne et al. (2007) we compare our model output with three satellite-based primary productivity estimates, developed by Behrenfeld and Falkowski (1997), Carr (2002) and Marra et al. (2003). As seen in Figure 7a, the Carr (2002) algorithm closely matches the overall production (61 GtC vs 63.4 GtC/yr) and time-varying pattern (correlation of 0.75). The modeled export diverges somewhat more from the observations (Figure 7b), being overly dominated by high productivity regions, the physical representation of which may be poorly resolved in our coarse model. Additionally, our model tends to concentrate production and export in subpolar regions during the strong spring bloom, while the satellite-based estimates show more productivity during summertime months.

3 Deconstructing the global response to aspects of iron limitation

BLING simulates global spatial and temporal variability of dissolved Fe concentrations throughout the ocean, which are then used to calculate Def_{Fe} . We explore the global biogeochemical response to physiological representations of iron limitation by starting with a version of the model in which the simulated iron concentrations have no effect on photosynthesis, and subsequently introduce an iron dependency to each of the three terms α^{chl} , θ_{max}^{Fe} and P_m^C , both alone and in combination. A model that ignores the effect of iron limitation on any one of the three relevant terms would use something close to the mean value for each, rather than removing the term altogether; we therefore ‘eliminate’ the effect of iron by replacing Def_{Fe} with the global mean value. This means that including the effect of iron will cause growth rates to increase in iron-rich regions, and to decrease in iron-poor regions, all else remaining equal. We refer to the run in which the simulated iron has no effect on growth as AllMean, and the run in which all three terms depend on the simulated iron as AllVar (note this is the configuration described in section 2g, above). The mean Def_{Fe} is determined from the final century of the AllVar run (equal to 0.4595). Intermediate between AllMean and AllVar are Var α , Var θ and VarLiebig, in which iron affects only one of α^{chl} ,

511 θ_{\max}^{Fe} and P_m^C , respectively, and Var α + θ , Var θ +Liebig and Var α +Liebig, in which all but one
 512 of the three parameters depends on the simulated iron concentrations. It is important to
 513 recognize that α^{chl} and θ_{\max}^{Fe} have numerically identical effects on I_k in our formulation (and
 514 given our parameter choices), such that their product essentially represents the efficiency with
 515 which incident light is harvested by the phytoplankton. Hence, we present the results for the
 516 two as interchangeable (with the exception of their impacts on chlorophyll, which differ).

517 The lower panels of Figure 7 show the global impact of including iron dependencies on
 518 primary production and export production. Unsurprisingly, the interhemispheric asymmetry in
 519 iron supply causes primary productivity to decrease in the iron-poor southern hemisphere, and
 520 to increase in the northern hemisphere, for all iron limited runs, relative to AllMean (Figure
 521 7c). All iron-dependent runs also show a slight decrease in primary productivity on the
 522 equator, though more pronounced is a meridional widening of the high-productivity zone.
 523 Meanwhile, changes in particle export follow a similar pattern but show extreme differences
 524 in the Southern Ocean – though striking, this simply follows from the nonlinear increases of
 525 biomass and particle export with increasing growth rates. However, a surprising response is
 526 evidenced in the relative sensitivities of different iron limitation terms. In the northern
 527 hemisphere, the subsequent inclusion of each additional iron dependency causes the export to
 528 increase, such that each term appears to be of roughly equivalent importance. In contrast,
 529 within the Southern Hemisphere, the inclusion of the light-harvesting efficiency terms (Var α
 530 and Var θ) only have an impact when VarLiebig is not included. All simulations including an
 531 iron-dependent light-saturated growth rate (VarLiebig, Var θ / α +Liebig and AllVar) are nearly
 532 indistinguishable. This begs the question, why does an iron dependency in the light-saturated
 533 growth rate (VarLiebig) overwhelm the iron dependency of the light harvesting efficiency
 534 (Var α and Var θ), and why is this so pronounced in the Southern Ocean?

535 To understand the results of the experiments we undertake a more detailed analysis, beginning
 536 with the impact of variable iron limitation on the surface PO_4 field. As shown in Figure 8b,
 537 the AllMean simulation greatly underestimates surface PO_4 , relative to observations, in the
 538 Southern Ocean, eastern equatorial Pacific, and subarctic Pacific. Including an iron
 539 dependency in any of the three photosynthesis terms, in any combination, reduces the total
 540 error relative to observations (see also Table 2). However, the strongest effect is clearly
 541 associated with the light-saturated photosynthesis term, VarLiebig (Figure 8d,f,h), which
 542 greatly outweighs the significance of the other terms – again, particularly in the Southern

Ocean, as shown in the zonal mean (Figure 7). This suggests that either our formulation has placed too much weight behind the VarLiebig term, or that the net result of including multiple limitations tends to largely eliminate the impacts of photosynthetic efficiency on the surface nutrient field.

The photosynthetic efficiency terms (Var α and Var θ) do have a significant impact on light limitation (Figure 9), as expected, causing changes that are of approximately the same magnitude as those of VarLiebig (Figures 9b vs. 9c). However, they are dominantly of the opposite *sign* of the VarLiebig changes. In the VarLiebig case (Figure 9d), the reduction of P_m^C within iron-limited domains actually causes a decrease in the severity of light limitation (e.g. in the Southern Ocean). Thus, if the ability to synthesize chlorophyll and photosynthetic reaction centers is unaffected by iron concentrations, the sole effect of iron limitation is to decrease the light-saturated photosynthesis rate P_m^C , thereby decreasing the demand for light. In contrast, including iron dependencies in only the photosynthetic efficiency terms (experiments Var α/θ and Var $\alpha+\theta$) clearly exacerbates light limitation in regions with low Def_{Fe} , more consistent with observations (Maldonado et al., 1999; Hiscock et al., 2008).

Nonetheless, in the global simulation, the effects of iron on photosynthetic efficiency and the effects of iron on the total growth rate (Figure 10) look very different. First, in the Southern Ocean, the impact of photosynthetic efficiency on light limitation is clearly significant when it acts alone, decreasing the light limitation term by up to ~25% (Figure 9, panels b and d). However, the importance of photosynthetic efficiency on the Southern Ocean is almost entirely muted when the light-saturated growth rate is also affected by iron (Figure 10, panels e and g). This is because the light limitation term of eq. (2), $P_m^C / \alpha^{chl} \theta_{max}^{Fe}$, becomes vanishingly small as iron becomes very limiting in the Liebig component of P_m^C , an effect that is further exaggerated due to the low temperatures of the Southern Ocean (making P_m^C even smaller). Thus, the tendency for photosynthetic efficiency to deteriorate under extreme iron limitation is ameliorated by the low energy demand at the very low inherent growth rates. In contrast, in relatively warm waters where iron is abundant, the light limitation term $P_m^C / \alpha^{chl} \theta_{max}^{Fe}$ is relatively large, providing increased leverage to variability of α^{chl} and θ_{max}^{Fe} and thereby accentuating iron-light colimitation. This is evident in the enhanced light limitation in the tropical Pacific, off equator, which persists when VarLiebig is included (Figure 9, panels b and d vs. e and g). In physiological terms, the inherent ability of phytoplankton to grow more

quickly in warm waters gives them a greater demand for usable electrons, and therefore makes them more dependent on efficient photosynthetic machinery. We point out that this prediction arises directly from our theoretically-based inclusion of iron limitation in the Geider photoadaptation framework; its relevance should be tested by field and laboratory experiments.

However, despite the fact that the tropical Pacific becomes much more light limited when photosynthetic efficiency depends on iron concentrations, this region actually experiences an increase in growth rates in these same simulations (Figure 10b,d). This occurs because overall growth rates are not just a function of light limitation but also of nutrient availability, which is modulated by ocean circulation and nutrient cycling, presenting non-local effects. In the tropical Pacific (off-equator), the supply of PO_4 to this otherwise P-starved region is increased by greater leakage from the equatorial Pacific, as the latter region becomes more iron limited (compare Figures 9b,d, 10b,d), an effect previously discussed by Dutkiewicz et al. (2005). Essentially, the increase of macronutrient abundance in this region, caused by iron limitation upstream, more than compensates for the enhanced light limitation in the simulations.

These nuances help to explain the finding, pointed out in Figure 7, that the effect of iron on photosynthetic efficiency is almost completely overwhelmed by that of the Liebig term, outside of the northern oceans. In these latter regions, greater iron availability allows phytoplankton to grow more quickly, making them more hungry for light and therefore more sensitive to the photosynthetic efficiency terms, as revealed by the responses to $\text{Var}\alpha$ and $\text{Var}\theta$. Meanwhile, near tropical upwellings, decreases in photosynthetic efficiency are counterbalanced by large increases in macronutrient supply, which end up dominating changes in growth rate. Finally, in the Southern Ocean, where phytoplankton are burdened by low temperatures and scarce iron, the low light-saturated photosynthesis rates mean that the plankton do not need a lot of light, and thus show little additional response to $\text{Var}\alpha$ and $\text{Var}\theta$. This leads to the remarkable paradox that when iron is most scarce, its effect on photosynthetic efficiency has the least impact on biogeochemistry.

Importantly, the greater impact of photosynthetic efficiency on production in the northern hemisphere (Figure 7) is not due to an overall increase in annually averaged growth rates (compare panels 10c and 10f). Instead, it acts through modulation of the seasonal cycle. As shown in Figure 11a, the annual cycle of productivity in the North Atlantic (70°W - 0° , 50°N - 65°N) reveals distinct impacts from all three limitation terms. All contribute to intensifying

the spring bloom and shifting it earlier, due to the relative abundance of iron resupplied from below by deep winter mixing, and to suppressing production during summer, due to more rapid nutrient depletion. Because of the strong degree of nonlinearity between growth and export, a more intense spring bloom produces a much higher annually integrated particle export. Surface chlorophyll (Figure 11b) shows a similar pattern, with the exception that increased growth rates in experiments including Var α are compensated by a lower chl:C ratio, so that α^{chl} has little impact on chlorophyll. In contrast, in the Southern Ocean (80°S-50°S), the inclusion of regionally dependent iron limitation suppresses growth rates, and prevents strong blooms. Inclusion of an iron dependency on the maximum light-saturated photosynthesis rate, in experiment Var Liebig (red line), has a large impact on the seasonal cycle, so that Var α +Liebig, Var θ +Liebig (light blue line) and AllVar (dashed black line) are essentially identical to VarLiebig. As discussed above, this reflects the relatively low utility of light to cells with low maximum photosynthesis rates, arising from the cold waters and perennial iron-limitation of P_m^C , so that photosynthetic efficiency has little role to play. Surface chlorophyll (Figure 11d) shows more of a temporal impact as iron deficiency is added, with the more iron-limited cases showing a dip in chlorophyll as iron limitation impedes chlorophyll synthesis during the very iron-depleted summer.

4 Conclusions

We have developed a simplified model of oceanic biogeochemical cycling built upon the photoadaptation model of Geider et al. (1997) and the biogeochemical algorithms of particle export developed by Dunne et al. (2005). The resulting model, BLING, simulates phytoplankton growth rates from instantaneous macronutrient and micronutrient concentrations, temperature, and light limitation. Then, through a parameterization of ecosystem processes, BLING uses those growth rates in order to determine biomass, uptake, dissolved organic matter production and the export of sinking particles. Embedded in a general circulation model of the ocean, BLING reproduces many features of the large-scale nutrient and chlorophyll fields, but because it uses relatively few prognostic tracers it can be run relatively cheaply.

We used this model to explore the impacts of variously applying iron dependencies to the light-saturated photosynthesis rate (P_m^C), the efficiency with which each unit of chlorophyll

produces usable electrons at low levels of light (α^{chl}), and the ability of the plankton to
 synthesize chlorophyll, $\theta_{\text{max}}^{\text{Fe}}$. In general, including iron-dependent photosynthesis terms
 reduced growth rates in macronutrient-rich regions (primarily the Southern Ocean, equatorial
 Pacific, and subarctic Pacific) and allowed macronutrients to leak to neighbouring
 oligotrophic regions, increasing growth rates there (Figure 10f). Including an iron dependency
 of P_m^C (experiments with VarLiebig) had the largest effect on all aspects of the simulation.
 This included a remarkably large effect on light limitation, through iron limitation of P_m^C ,
 shrinking the first term of eq. (2), $P_m^C / \alpha^{\text{chl}} \theta_{\text{max}}^{\text{Fe}}$ and thereby mitigating iron-light colimitation.
 In physiological terms, this represents a reduction in the usefulness of light to a phytoplankton
 community whose light-saturated growth rates are severely restricted by a lack of Fe, even
 when the ability to harvest light is itself hampered by iron-limited decreases of α^{chl} and/or
 $\theta_{\text{max}}^{\text{Fe}}$. This general tendency seems to be supported by at least one laboratory experiment,
 carried out with a *Chaetoceros* diatom (Davey and Geider, 2001), for which changes in
 chlorophyll-normalized P_m^C (i.e. P_m^B) under varying iron limitation were of approximately the
 same magnitude as α^{chl} , so that $P_m^C / \alpha^{\text{chl}} \theta_{\text{max}}^{\text{Fe}}$ remained approximately constant. In contrast,
 where P_m^C increases as a result of abundant iron and/or PO_4 , the importance of iron
 dependencies on α^{chl} and $\theta_{\text{max}}^{\text{Fe}}$ also increase, since the term $P_m^C / \alpha^{\text{chl}} \theta_{\text{max}}^{\text{Fe}}$ becomes relatively
 large. Temperature has a related effect on light limitation in the simulations, since at high
 temperature, rapid light-saturated photosynthesis rates increase the demand for light, leading
 to a greater importance of iron-light colimitation in tropical waters. In contrast, the low
 inherent growth rates in cold waters of the Southern Ocean reduced the demand for photons,
 such that the impact of iron on photosynthetic efficiency was relatively unimportant.

Figure 12 illustrates the effect of this interaction between terms on the export production, with
 panel (a) showing the linear sum of the changes in export production expected from
 experiments Var α/θ and VarLiebig, and panel (b) showing the changes in export production
 actually simulated in experiment AllVar. The difference between these two panels reveals the
 impact of VarLiebig on the impact of the photosynthetic efficiency. In most of the world, the
 impact of iron on photosynthetic efficiency is muted by the effect on P_m^C . Only in parts of the
 northern hemisphere, where high seasonal abundances of iron drive all three terms to increase,
 does the amplitude of change in the AllVar model (panel b) exceed the linear sum (panel a).
 We would emphasize that the degree to which these predictions hold depends on the details of

our formulation and choice of parameters – the model presented here is certainly wrong in many respects. Nonetheless, these clear predictions offer a target that iron enrichment experiments can test by deliberately isolating the effects of temperature, macronutrient limitation, and light.

The correlation and regression coefficients for the range of experiments (Table 2) showed little improvement when $\text{Var}\alpha$ was included, for which we offer an explanation here. Much of the conceptual basis for this paper is based on pulsed iron additions applied to bottle incubations or mesoscale patches, which reflect the response of a given species or community to changes in iron availability. However, observations of natural communities across gradients of iron availability in the Southern Ocean suggest that community-wide responses to long-term iron limitation may diverge from the more clear-cut, short-term responses of iron-fertilization experiments. In particular, Hopkinson et al. (2007) showed that changes in α^{chl} between naturally iron-rich shelf and iron-poor open-ocean waters had no clear relationship to iron availability.

We propose that the long-term adjustment of ocean ecosystems to the available iron supply differs from the short-term response of biota to pulsed iron enrichments, in terms of α^{chl} . The tendency for communities to become dominated by small plankton under iron-limitation, simply due to diffusion effects (Morel et al., 1991), will serendipitously increase α^{chl} , since small plankton have inherently more efficient photosynthetic machinery due to reduced ‘packaging effects’ (Greene et al., 1991). Thus, we speculate that even though many phytoplankton (particularly diatoms) can increase their photosynthetic efficiencies given sufficient iron (Strzepek and Harrison, 2004), the phytoplankton that dominate iron-limited systems have inherently high photosynthetic efficiencies, so that the global distribution of iron is not strongly correlated with community α^{chl} . The fact that our experiments show clear improvements in the simulations of global macronutrients (Table 2) when both P_m^C and θ vary (experiment $\text{Var}\theta+\text{Liebig}$), but not when α^{chl} is allowed to vary as well (experiment AllVar), would be consistent with a weak dependence of α^{chl} on iron across natural communities.

In closing, our results suggest that models which do not parameterize the effects of iron availability on photosynthetic efficiency are not missing much in terms of simulating global-scale biogeochemistry, due to the dominant impact of iron availability on the light-saturated photosynthesis rate. However, they are likely to impact more subtle features of global

699 simulations, such as the distribution of chlorophyll, and the seasonal cycle of primary
700 production, particularly spring blooms in the North Atlantic.

701

702 **Acknowledgements**

703 We thank Jorge Sarmiento, Charles Stock and Patrick Schultz for helpful discussions,
704 Stephanie Henson for providing the SeaWifs climatology, and Christopher Measures for
705 sharing the iron concentration data. Adrian Marchetti and Julie Granger commented on an
706 early version of the draft.

707

707 **References**

- 708 Agawin, N. S. R., Duarte, C.M, and Agusti,S.: Nutrient and temperature control of the
709 contribution of picoplankton to phytoplankton biomass and production, *Limnol. Oceanogr.*,
710 45, 591– 600, 2000.
- 711 Anderson, L.A : On the hydrogen and oxygen content of marin phytoplankton. *Deep Sea Res.*
712 Pt. I, 42, 1675-1680, 1995.
- 713 Aumont, O. and Bopp, L.: Globalizing results from in-situ iron fertilization studies, *Global*
714 *Biogeochem. Cy.*, 20, GB2017, doi:10.1029/2005GB002591, 2006.
- 715 Barbeau, K., Rue, E.L, Bruland, K.W., and Butler,A.: Photochemical cycling of iron in the
716 surface ocean mediated by microbial iron(III)-binding ligands. *Nature*, 413: 409-413, 2001.
- 717 Barbeau, K., Rue, E.L. Trick. C.L., Bruland, K.W. and Butler,A.: Photochemical reactivity of
718 siderophores produced by marine heterotrophic bacteria and cyanobacteria based on Fe(III),
719 *Limnol Oceanogr.*, 48, 1069-1078, 2003.
- 720 Behrenfeld, M. J., and Falkowski, P.G.: Photosynthetic rates derived from satellite-based
721 chlorophyll concentration, *Limnol. Oceanogr.*, 42, 1 –20, 1997.
- 722 Behrenfeld, M.J., Boss, E., Siegel, D.A. and Shea, D.M.: Carbon-based ocean productivity
723 and phytoplankton physiology from space, *Global Biogeochemical Cy.*, GB10006,
724 doi:10.1029/2004GB002299, 2005.
- 725 Boss, E. and coauthors: Observations of pigment and particle distributions in the western
726 North Atlantic from an autonomous float and ocean color satellite, *Limnol. Oceanogr.*, 53,
727 2112-2122, 2008.
- 728 Boyd, P.W. and coauthors: The evolution and termination of an iron-induced mesoscale
729 bloom in the northeastern subarctic Pacific, *Limnol. Oceanogr.*, 50, 1872-1886, 2005.
- 730 Boyd, P.W. and coauthors: Mesoscale iron enrichment experiments 1993-2005: Synthesis and
731 future directions, *Science*, 315, 612 – 617, 2007.
- 732 Carr, M.-E.: Estimation of potential productivity in Eastern Boundary Currents using remote
733 sensing, *Deep Sea Res.*, Part II, 49, 59–80, 2002.
- 734 Davey, M. and Geider, R.J.: Impact of iron limitation on the photosynthetic apparatus of the
735 diatom *Chaetoceros muelleri* (bacillariophyceae), *J. Phycol.*, 37, 987-1000, 2001.

736 Doney, S.C., Lindsay, K., Fung, I. and John, J.: Natural variability in a stable, 1000- Yr global
737 coupled carbon-climate model simulation, *J. Climate*, 19, 3033-3054, 2006.

738 Dugdale, R.C. and Goering, J.J.: Uptake of new and regenerated forms of nitrogen in primary
739 productivity, *Limnol. Oceanogr.*, 12, 196-206, 1967.

740 Dunne, J.P., Armstrong, R.A., Gnanadesikan, A. and Sarmiento, J.L.: Empirical and
741 mechanistic models of the particle export ratio, *Global Biogeochemical Cycles*, 19, GB4026,
742 doi:10.1029/2004GB002390, 2005.

743 Dunne, J. P., Sarmiento, J.L. and Gnanadesikan, A.: A synthesis of global particle export
744 from the surface ocean and cycling through the ocean interior and on the seafloor. *Global*
745 *Biogeochemical Cycles*, 21, GB4006, doi:10.1029/2006GB002907, 2007.

746 Dusenberry, J., Olson, R.J. and Chisholm, S.W.: Photoacclimation kinetics of single-celled
747 fluorescence in laboratory and field populations of *Prochlorococcus*, *Deep Sea Res. I*, 48,
748 1443-1458, 2001.

749 Dutkiewicz, S., Follows, M.J. and Parekh, P.: Interactions of the iron and phosphorus cycles:
750 A three-dimensional model study, *Global Biogeochemical Cy.*, 19, GB1021,
751 doi:10.1029/2004GB002342, 2005.

752 Eppley, R. W.: Temperature and phytoplankton growth in the sea, *Fish. Bull.*, 70, 1063-1085,
753 1972.

754 Frennette, J.J., Demers, S., Legendre, L. and Dodson, J.: Lack of agreement among models
755 for estimating the photosynthetic parameters, *Limnol. Oceanogr.*, 38, 679-687, 1993.

756 Geider, R.J., MacIntyre, H.L. and Kana, T.M.: Dynamic model of phytoplankton growth and
757 acclimation: Response of the balanced growth rate and chlorophyll a to carbon ratio to light,
758 nutrient limitation and temperature, *Mar. Ecol. Prog. Ser.*, 148, 187-201, 1997.

759 Gent, P.J. and McWilliams, J.C.: Isopycnal mixing in ocean circulation models, *J. Phys.*
760 *Oceanogr.*, 20, 150-155, 1990.

761 Ginoux, P., Prospero, J.M., Torres, O., and M. Chin, M.: Long-term simulation of global dust
762 distribution with the GOCART model: correlation with North Atlantic Oscillation,
763 *Environmental Modelling and Software*, 19, 113-128, 2004.

764 Gnanadesikan A., and co-authors: GFDL's CM2 Global Coupled Climate Models- Part 2: The
765 baseline ocean simulation, *J. Climate*, 19, 675-697, 2006.

766 Gnanadesikan, A., Dunne, J.P., Key, R.M., Matsumoto, K., Sarmiento, J.L., Slater, R.D. and
 767 Swathi, P.S.: Oceanic ventilation and biogeochemical cycling: Understanding the physical
 768 mechanisms that produce realistic distributions of tracers and productivity. *Global*
 769 *Biogeochemical Cycles*, 18(4), GB4010, doi:10.1029/2003GB002097, 2004.

770 Gnanadesikan, A., Slater, R.D., Gruber, N. and Sarmiento, J.L.: Oceanic vertical exchange and
 771 new production, a comparison between models and data, *Deep Sea Res. Pt. II*, 49, 363-401,
 772 2002.

773 Gnanadesikan, A., Griffies, S.M., and B.L. Samuels, B.L.: Effects in a climate model of slope
 774 tapering on neutral physics schemes, *Ocean Modelling*, 16, 1-16,
 775 doi:10.1016/j.ocemod.2006.06.004, 2007.

776 Granger, J. and Price, N.M.: The importance of siderophores in the iron nutrition of
 777 heterotrophic marine bacteria, *Limnol. Oceanogr.*, 44, 541-555, 1999.

778 Greene, R.M., Geider, R.J., and Falkowski, P.G: Effect of iron limitation on photosynthesis in
 779 a marine diatom, *Limnol. Oceanogr.*, 36, 1772-1782, 1991.

780 Griffies, S.M. and coauthors: Coordinated Ocean-ice Reference Experiments (COREs), *Ocean*
 781 *Modelling*, 26, 1-46, 2009.

782 Griffies, S.M. Gnanadesikan, A., Dixon, K.W., Dunne, J.P., Gerdes, R., Harrison, M.J.,
 783 Rosati, A., Russell, J. L., Samuels, B. L., Spelman, M.J., Winton, M. and Zhang, R. 2005:
 784 Formulation of an ocean model for global climate simulations. *Ocean Science*, 1, 45-79, 2005.

785 Hiscock, M.R., Lance, V.P., Apprill, A, Bidigare, R.R, Johnson, Z.I., Mitchell, B.G. Smith,
 786 W.O., and Barber, R.T.: Photosynthetic maximum quantum yield increases are an essential
 787 component of the Southern Ocean phytoplankton response to iron, *Proc. Natl. Acad. Sci.*, 105,
 788 4775-4780, 2008.

789 Honeyman, B., Balistrieri, L. and Murray, J.: Oceanic trace metal scavenging and the
 790 importance of particle concentration, *Deep Sea Res.*, Pt I, 35, 227-246, 1988.

791 Hopkinson, B.M., Mitchell, B.G. Reynolds, R.A., Wang, H., Selph, K.E., Measures, C.I.,
 792 Hewes, C.D., Holm-Hansen, O., and Barbeau, K.A.: Iron limitation across chlorophyll
 793 gradients in the southern Drake Passage: Phytoplankton responses to iron addition and
 794 photosynthetic indicators of iron stress. *Limnol. Oceanogr.*, 52(6), 2540-2554, 2007.

795 Hutchins, D.A., DiTullio, G.R., Zhang, Y. and Bruland, K.W.: An iron limitation mosaic in
 796 the California upwelling regime, *Limnol. Oceanogr.* 43, 1037-1054, 1998.

797 Johnson, K., Gordon, R.M. and Coale, K.H.: What controls dissolved iron concentrations in
 798 the world ocean? *Mar. Chem.*, 57, 137-161, 1997.

799 Kriest, I. and Oschlies, A. : On the treatment of particulate organic matter sinking in large-
 800 scale models of marine biogeochemical cycles, *Biogeosciences*, 5, 55-72, 2008.

801 Lam, P. J., Bishop, J. K. B. , Henning, C. C. , Marcus, M. A. , Waychunas, G. A. and Fung,
 802 I.Y.: Wintertime phytoplankton bloom in the subarctic Pacific supported by continental
 803 margin iron, *Global Biogeochem. Cycles*, 20, GB1006, doi:10.1029/2005GB002557, 2006.

804 Large, W., McWilliams, J.C., and Doney, S.C.: Oceanic vertical mixing: A review and a
 805 model with a nonlocal boundary mixing parameterization. *Rev. Geophys.*, 32, 363–403, 1994.

806 Mahowald, N. M., Baker, A.R., Bergametti, G., Brooks, N., Duce, R.A., Jickells, T.D.,
 807 Kubilay, N., Prospero, J.M. and I. Tegen, I.: Atmospheric global dust cycle and iron inputs to
 808 the ocean, *Global Biogeochem. Cycles*, 19, GB4025, doi:10.1029/2004GB002402, 2005.

809 Maldonado, M.T. , Boyd, P.W., Harrison, P.J., and Price, N.M.: Co-limitation of
 810 phytoplankton growth by light and Fe during winter in the NE subarctic Pacific Ocean, *Deep-*
 811 *Sea Research II*, 46, 2475-2485, 1999.

812 Manizza, M., Le Quere, C. Watson, A. J. and Buitenhuis, E.T.: Bio-optical feedbacks among
 813 phytoplankton, upper ocean physics and sea-ice in a global coupled model, *Geophysical*
 814 *Research Letters*, 32, L05603, doi:10.1029/2004GL020778., 2005.

815 Marchetti, A., Juneau, P., Whitney, F.A., Wong, C.S. and Harrison, P.J., Phytoplankton
 816 processes during a mesoscale iron enrichment in the NE subarctic Pacific: Part III- primary
 817 productivity, *Deep Sea Res. II*, 53, 2131-2151, 2006a.

818 Marchetti, A., Maldonado, M.T., Lane, E.S., Harrison, P.J.: Iron requirements of the pennate
 819 diatom *Pseudo-nitzschia*: Comparison of oceanic (high-nitrate, low-chlorophyll waters) and
 820 coastal species, *Limnol. Oceanogr.*, 51, 2092-2101, 2006b.

821 Marchetti, A. and Harrison, P.J.: Coupled changes in the cell morphology and the elemental
 822 (C,N, and Si) composition of the pennate diatom *Pseudo-nitzschia* due to iron deficiency,
 823 *Limnol. Oceanogr.*, 52(5), 2270-2284, 2007.

824 Marchetti, A., Parker, M.S., Moccia, L.P., Lin, E.O., Arrieta, A.L., Ribalet, F., Murphy,
825 M.E.P., Maldonado, M.T., and Armbrust, E.V.: Ferritin is used for iron storage in bloom-
826 forming marine pinnate diatoms, *Nature*, 457, 467-470, 2009.

827 Marra, J., Ho, C., and Trees, C.C.: An alternative algorithm for the calculation of primary
828 productivity from remote sensing data, LDEO Tech. Rep. LDEO-2003-1, Lamont Doherty
829 Earth Obs., Palisades, N. Y, 2003.

830 Measures, C.I., Landing, W.M., Brown M.T., and Buck, C.S.: High resolution Al and Fe data
831 from the Atlantic Ocean CLIVAR-CO2 Repeat Hydrography A16N transect: Extensive
832 linkages between atmospheric dust and upper ocean geochemistry, *Global Biogeochem.*
833 *Cycles*, 22, GB1005, doi:10.1029/2007GB003042, 2008.

834 Milligan, A. J. and Harrison, P. J: Effects of non-steady-state iron limitation on nitrogen
835 assimilatory enzymes in the marine diatom *Thalassiosira weissflogii* (bacillariophyceae), *J.*
836 *Phycol.* 36, 78-86, 2000.

837 Moore, J.K., Doney, S.C., and K. Lindsay, K.: Upper ocean ecosystem dynamics and iron
838 cycling in a global 3-D model, *Global Biogeochem. Cycles*, 18, GB4028,
839 doi:10.1029/2004GB002220, 2004.

840 Moore, J.K. and Braucher, O.: Sedimentary and mineral dust sources of dissolved iron to the
841 world ocean, *Biogeosciences*, 5, 631-656, 2008.

842 Morel, F.M.M., Hudson, R.J.M., and Price, N.M.: Limitation of productivity by trace metals
843 in the sea, *Limnol. Oceanogr.*, 36, 1742-1755, 1991.

844 Najjar, R.G. and Orr, J.C.: Biotic HOWTO, Internal OCMIP Report, LSCE/CEA Saclay, Gif-
845 sur-Yvette, France, 15pp., 1999.

846 Parekh, P., Follows, M.J., and Boyle, E.A.: Decoupling of iron and phosphate in the global
847 ocean, *Global Biogeochem. Cy.*, 19, GB2020, 10.1029/2004GB002280, 2005.

848 Price, N.M., Andersen, L.F., and Morel, F.M.M.: Iron and nitrogen limitation of equatorial
849 Pacific plankton, *Deep Sea Res. I*, 38, 1361-1378, 1991.

850 Raven, J.: Predictions of Mn and Fe use efficiencies of phototropic growth as a function of
851 light availability for growth and of C assimilation pathway, *New Phytol.*, 116, 1-18, 1990.

852 Rue, E.L. and Bruland, K.W.: Complexation of iron(III) by natural organic ligands in the
853 Central North Pacific as determined by a new competitive ligand equilibration / adsorptive
854 cathodic stripping voltametric method, *Mar. Chem.*, 50, 117–138, 1995.

855 Simmons, H.L., Jayne, S.R., St. Laurent, L.C. and Weaver, A.J.: Tidally-driven mixing in a
856 numerical model of the ocean general circulation, *Ocean Modelling*, 6, 245-263, 2004.

857 Strzepek, R.F. and Harrison, P.J.: Photosynthetic architecture differs in coastal and oceanic
858 diatoms, *Nature*, 431, 689-692, 2004.

859 Sunda, W.G. and Huntsman, S.A.: Interrelated influence of iron, light, and cell size on
860 marine phytoplankton growth, *Nature*, 390, 389-392, 1997.

861 Tagliabue, A., and Arrigo, K.R.: Iron in the Ross Sea: 1. Impact on CO₂ fluxes via variation
862 in phytoplankton functional group and non-Redfield stoichiometry, *J. Geophys. Res.*, 110,
863 C03009, doi:10.1029/2004JC002531, 2005.

864 Timmermans, K.R., van der Wagt, B. Veldhuis, M.J.W., Maatman, A. and De Baar, H.J.W.:
865 Physiological responses of three species of marine pico-plankton to ammonium, phosphate,
866 iron and light limitation, *J. Sea Res.*, 53, 109-120, 2005.

867 Tortell, P.D., Maldonado, M.T., Granger, J. and Price, N.M.: Marine bacteria and
868 biogeochemical cycling of iron in the oceans, *FEMS Microbio. Ecol.*, 29, 1-11, 1999.

869 Trick, C.G., Andersen, R.J., Price, N.M., Gillam, A. and Harrison, P.J.: Examination of
870 hydroxamate-siderophore production by neritic eukaryotic marine phytoplankton, *Mar. Biol.*,
871 75,9-17, 1983.

872 Weber, L., Volker, C., Schartau, M. and Wolf-Gladrow, D.: Modeling the biogeochemistry
873 and speciation of iron at the Bermuda Atlantic Time Series site, *Global Biogeochemical*
874 *Cycles*, 19, GB1019, 2005.

875 Wu, J., Boyle, E., W. Sunda, W. and Wen, L.-S.: Soluble and colloidal iron in the
876 oligotrophic North Atlantic and North Pacific, *Science*, 293, 847-849, 2001.

877

878

<i>Variable</i>	<i>Description</i>	<i>Reference or Initial guess</i>	<i>Final Value</i>	<i>Units</i>
K_{Eppley}	Temperature dependence of growth	0.063 (Eppley, 1972)	0.063	deg C ⁻¹
$\gamma_{\text{irr_mem}}$	Photoadaptation time constant	1	1	d ⁻¹
P_0^c	Maximum carbon-specific growth rate at 0 C	1.00E-05	1.00E-05	s ⁻¹
α_{max}	Quantum yield under low light, abundant iron	6.4-100 (Geider, 1997)	73.6	$\mu\text{g C g}^{-1} \text{ chl m}^2 \text{ W}^{-1} \text{ s}^{-1}$
α_{min}	Quantum yield under low light, extreme iron limitation	6.4-100 (Geider, 1997)	18.4	$\mu\text{g C g}^{-1} \text{ chl m}^2 \text{ W}^{-1} \text{ s}^{-1}$
$\theta_{\text{max-hi}}$	Maximum Chl:C ratio, abundant iron	0.007-0.072 (Geider, 1997)	0.04	g Chl g C ⁻¹
$\theta_{\text{max-lo}}$	Maximum Chl:C ratio, extreme iron limitation	0.007-0.072 (Geider, 1997)	0.01	g Chl g C ⁻¹
γ_{biomass}	Biomass adjustment time constant	0.5	0.5	d ⁻¹
k_{Fe}	Dissolved Fe uptake half-saturation constant	0.8	0.8	nmol kg ⁻¹
k_{PO_4}	PO ₄ uptake half-saturation constant	0.2	0.1	$\mu\text{mol kg}^{-1}$
Fe:P_{max}	Maximum Fe:P uptake ratio	4.24	2.968	mmol Fe mol P ⁻¹
$k_{\text{Fe:P}}$	Half-saturation cellular Fe:P	1.06	0.742	mmol Fe mol P ⁻¹
λ_0	Carbon-specific phytoplankton mortality rate	0.19 (Dunne et al., 2005)	0.19	d ⁻¹
P^*	Pivotal phytoplankton biomass	0.018 (Dunne et al., 2005)	0.018	$\mu\text{mol P kg}^{-1}$
K_{remin}	Temperature dependence of particulate production	-0.032 (Dunne et al., 2005)	-0.032	deg C ⁻¹
ϕ_{DOP}	Fraction of non-particulate uptake converted to DOM	0.1	0.1	unitless (fraction)
γ_{DOP}	Decay timescale of DOM	0.25	0.25	y ⁻¹
C:P	Carbon to Phosphorus ratio in organic matter	106 (Anderson, 1995)	106	mol C mol P ⁻¹
$\text{O}_2\text{:P}$	O ₂ :P for photosynthesis and respiration	150 (Anderson, 1995)	150	mol O ₂ mol P ⁻¹
wsink_{0z}	Depth at which sinking rate starts increasing	80	80	m
wsink_0	Initial sinking rate	16	16	m d ⁻¹
$\text{wsink}_{\text{acc}}$	Acceleration rate of sinking with depth	0.05	0.05	d ⁻¹
γ_{POP}	Remineralization rate of sinking POM	0.12	0.12	d ⁻¹
k_{O_2}	Half-saturation constant for aerobic respiration	20	20	$\mu\text{mol kg}^{-1}$
$\text{remin}_{\text{min}}$	Minimum anaerobic respiration rate	0.3	0.3	unitless (fraction)
$\text{O}_2\text{-min}$	Minimum O ₂ concentration for aerobic respiration	1	1	$\mu\text{mol kg}^{-1}$
Ligand	Ligand concentration	1 (Parekh et al., 2005)	1	nmol kg ⁻¹
Fe:P_{sed}	Fe:P for sedimentary iron source	.072 (Elrod et al., 2004)	0.0106	mol Fe mol P ⁻¹
$K_{\text{FeL}_{\text{eq-max}}}$	Maximum Fe-ligand stability constant	1e10-1e13 (Parekh et al., 2004)	8.0E+10	kg mol lig ⁻¹
$K_{\text{FeL}_{\text{eq-min}}}$	Minimum Fe-ligand stability constant	4.00E+10	8.0E+09	kg mol lig ⁻¹
$K_{\text{FeL}_{\text{eq-irr}}}$	Irradiance scaling term for Kfe	1	0.10	W m ⁻²
$K_{\text{FeL}_{\text{eq-Femin}}}$	Low-Fe threshold for reduced stability constant	0.05	0.05	nmol kg ⁻¹
$k_{\text{Fe}_{\text{org}}}$	Organic-matter dependent scavenging rate	3	0.5	gC ⁻¹ m ³ d ⁻¹
$k_{\text{Fe}_{\text{inorg}}}$	Inorganic scavenging rate	3000	1000.00	d ⁻¹ nmol Fe ⁻⁵ kg ⁵

Table 1. Parameters used in BLING for the experiments shown here. Reference values are given, where appropriate, in italics. Otherwise, the initial guess is shown.

Table 2. Correlation, regression (italicized) coefficients and RMS errors (in bold) for the output of the model suite used here.

Corr, <i>Reg</i> Err	All Mean	Var α	Var θ	Var $\alpha+$ Var θ	Var Liebig	Var $\theta+$ Liebig	Var $\alpha+$ Liebig	AllVar
Annual Mean PO ₄	0.74 <i>0.51</i> 0.41	0.85 <i>0.65</i> 0.33	0.85 <i>0.65</i> 0.33	0.90 <i>0.76</i> 0.26	0.94 <i>0.91</i> 0.20	0.93 <i>0.89</i> 0.20	0.93 <i>0.89</i> 0.20	0.93 <i>0.89</i> 0.20
Annually varying PO ₄	0.71 <i>0.52</i> 0.44	0.81 <i>0.66</i> 0.36	0.81 <i>0.66</i> 0.35	0.88 <i>0.76</i> 0.29	0.92 <i>0.89</i> 0.23	0.91 <i>0.87</i> 0.22	0.91 <i>0.87</i> 0.22	0.91 <i>0.87</i> 0.23
Minimum PO ₄	0.49 <i>0.28</i> 0.48	0.71 <i>0.50</i> 0.37	0.71 <i>0.50</i> 0.37	0.81 <i>0.68</i> 0.27	0.86 <i>0.92</i> 0.18	0.85 <i>0.93</i> 0.19	0.85 <i>0.93</i> 0.19	0.85 <i>0.93</i> 0.19
Annual Mean log(Chl)	0.92 <i>1.11</i>	0.87 <i>1.09</i>	0.94 <i>1.09</i>	0.87 <i>1.02</i>	0.92 <i>0.94</i>	0.94 <i>0.96</i>	0.84 <i>0.88</i>	0.86 <i>0.90</i>
Zonal Mean PP (vs. Carr)	0.63	0.68	0.68	0.72	0.78	0.76	0.76	0.75
Zonal Mean PE (vs. Carr)	0.40	0.45	0.45	0.47	0.50	0.47	0.47	0.44

885

886 Figure 1. Conceptual map of the Biogeochemistry with Light Iron Nutrients and Gas model.
887 Prognostic tracers are shown as squares with solid outlines. Relevant environmental state
888 variables are shown as circles. Diagnostic quantities are shown as squares with dashed
889 outlines, where Chl is chlorophyll and Biom is biomass. The suite of plankton growth
890 calculations are represented by the green oval. Solid lines show fluxes of prognostic
891 quantities. Dashed lines (terminated by filled circles) indicate important interdependencies,
892 with the arrow pointing toward the dependent variable.

893

894 Figure 2: Photosynthesis rate at 20 °C as a function of light intensity (I), for a variety of
895 nutrient availabilities, with all three iron dependent terms. The heavy solid line represents
896 PO₄ and Fe replete conditions. Other solid lines show PO₄ replete photosynthesis rates at two
897 limiting Fe concentrations, while dashed lines show Fe replete photosynthesis rates at two
898 limiting PO₄ concentrations. The dotted line shows photosynthesis rates when both PO₄ and
899 Fe are limiting. Note that the approach to light-saturated photosynthesis rates is more gradual
900 when iron is limiting, due to the reduction of photosynthetic efficiency.

901

902 Figure 3: Particle fluxes in the BLING model. (a) Profile of particle flux compared with
903 Martin et al. (1987) and OCMIP2 particle flux curves. (b) Log of remineralization rate (%
904 production/m) compared with previous work. (c) Ratio of sinking particulate material to
905 primary production using this formulation, compared with observations from Dunne et al.
906 (2005).

907

908 Figure 4: Macronutrient simulation in BLING (AllVar experiment). (a) Annual mean PO₄
909 concentration from model. (b) Annual mean average macronutrient concentration from
910 observations (WOA01). (c) Annual range of PO₄ concentrations, 1 s.d., from model. (d)
911 Annual range of average macronutrient concentration from observations (WOA01).

912

913 Figure 5: Surface chlorophyll, in mg/m³, simulated by BLING (AllVar experiment) compared
914 with satellite observations. (a) Annual mean chlorophyll, from model. (b) Observed

chlorophyll, from SeaWifs (average). (c) Annual cycle of zonally averaged chlorophyll, model. (d) Annual cycle of zonally averaged chlorophyll, SeaWifs climatology (average). Note that the SeaWifs zonal average includes coastal regions with high chlorophyll concentrations, not captured by the model, which is therefore biased low.

Figure 6: Iron simulation in the BLING model (AllVar experiment). (a) Annual average surface iron concentration in nM. Symbols from the compilation of Moore and Braucher (2008), and represent discrete measurements, rather than annual averages. (b) Annual range of modeled iron concentrations, in nM (difference between local maximum and minimum). (c) Iron along the A16N section in the central Atlantic, symbols from the observations of Measures et al. (2008). (d) Annually averaged iron deficiency term $DefFe$ (equation 4).

Figure 7: Comparison between modeled and satellite-based estimates of primary productivity and particle export (units of $GtC/deg/yr$) for AllVar (top panels) and the full suite of experiments (lower panels). Plots show annually integrated values, correlations are for time varying values. (a,b) AllVar vs satellite-based estimates. (b) AllVar compared to the iron-dependency experiments, as described in the text.

Figure 8: Impact of including iron dependency terms on global, annual mean surface dissolved PO_4 concentrations (in μM). Panels a and g show simulated concentrations, whereas panels b-f and h show differences between the experiment indicated and the average macronutrient, calculated from observations (WOA01).

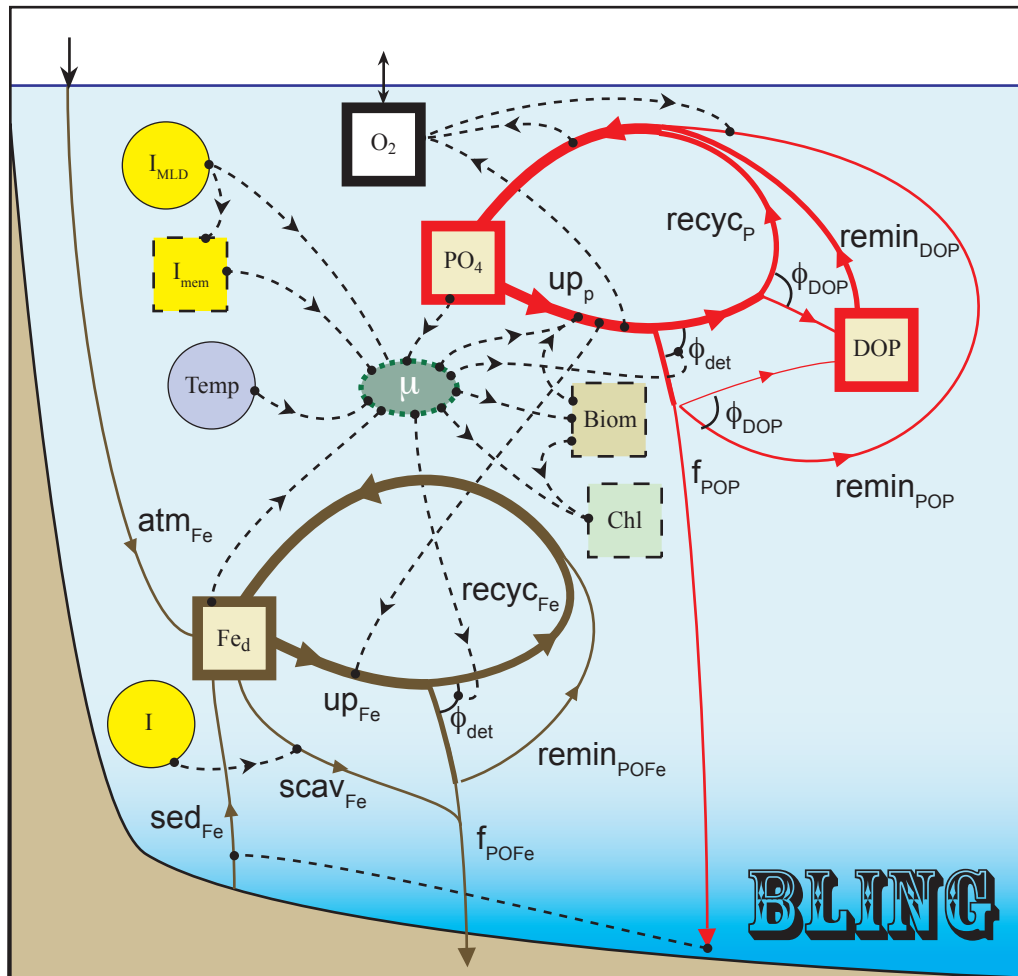
Figure 9: Impact of including iron dependency terms on light limitation (where 1 is no light limitation), vertically-weighted by phosphorus uptake rates. Panels a and f show simulated concentrations, whereas panels b-e and g show differences between the experiment indicated and the AllMean experiment, such that red colours indicate less light-limitation than AllMean, while blue colours indicate more-light limitation.

Figure 10: Impact of including iron dependency terms on growth rates, vertically-weighted by phosphorus uptake rates. Panels a and f show simulated rates (d-1), whereas panels b-e and g show differences between the experiment indicated and the AllMean experiment as a ratio, such that red colours indicate faster growth rates and blue colours indicate slower growth rates.

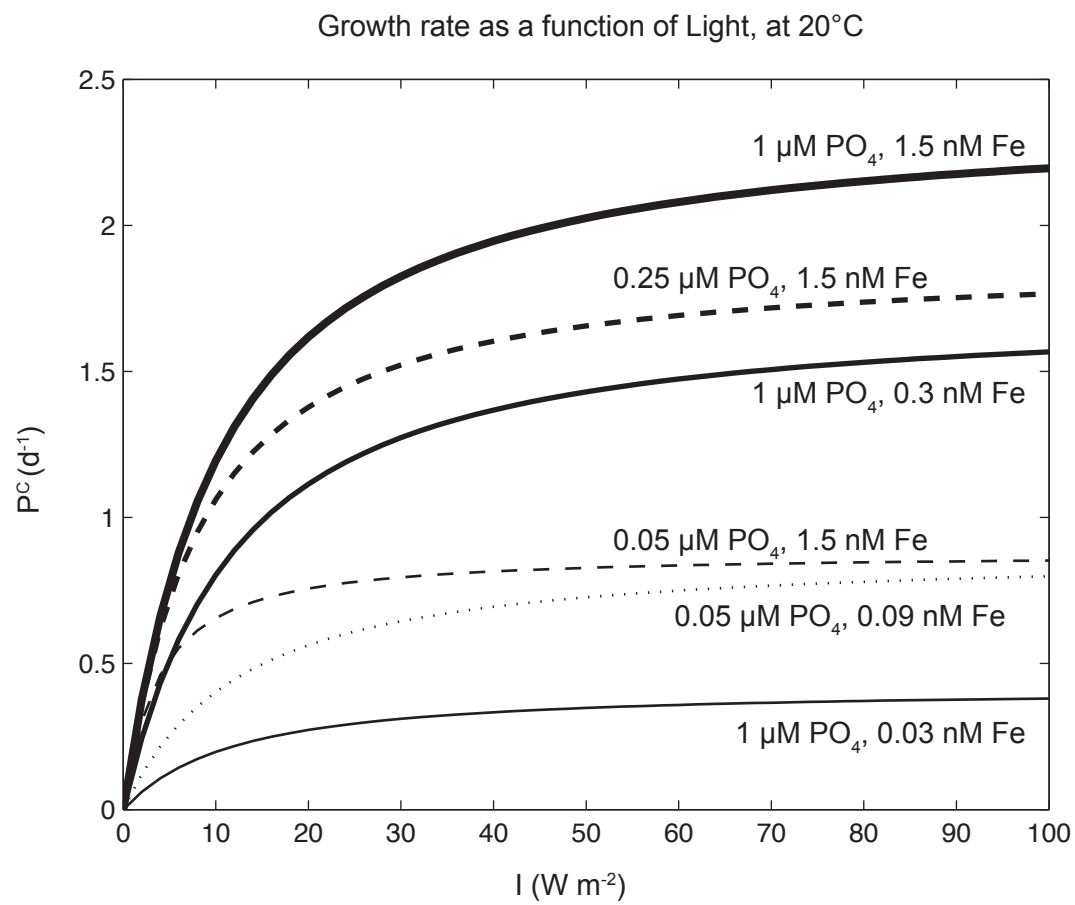
Figure 11: Impact of including iron dependency terms on the seasonal cycles of export production at 80m and surface chlorophyll. (a) Particle export in GtC/yr, subpolar North Atlantic (70W-0W,50-65N). Annually integrated values shown in parentheses. (b) Surface chlorophyll in mg/m³, subpolar North Atlantic. (c) Particle export in GtC/yr, subpolar/polar Southern Ocean (80S-50S). Annually integrated values shown in parentheses. (d) Surface chlorophyll in mg/m³, subpolar Southern Ocean.

Figure 12: Interactive effects of photosynthetic terms on global carbon export production (vertical flux at 100m). (a) The linear sum of changes caused by photosynthetic efficiency terms and the light-saturated photosynthesis term, i.e. $(\text{Var}\alpha + \theta - \text{AllMean}) + (\text{VarLiebig} - \text{AllMean})$. (b) The actual simulated change in export when all three terms are simultaneously included, i.e. $\text{AllVar} - \text{AllMean}$. If the terms operated independently, the two panels would be identical. Where the amplitude is reduced in (b) relative to (a), a decrease in the light-saturated photosynthesis rates is reducing the sensitivity to photosynthetic efficiency. Conversely, where changes in (b) are amplified relative to (a), an increase in light-saturated photosynthesis rates is enhancing the sensitivity to photosynthetic efficiency, so that the net result is larger than otherwise expected.

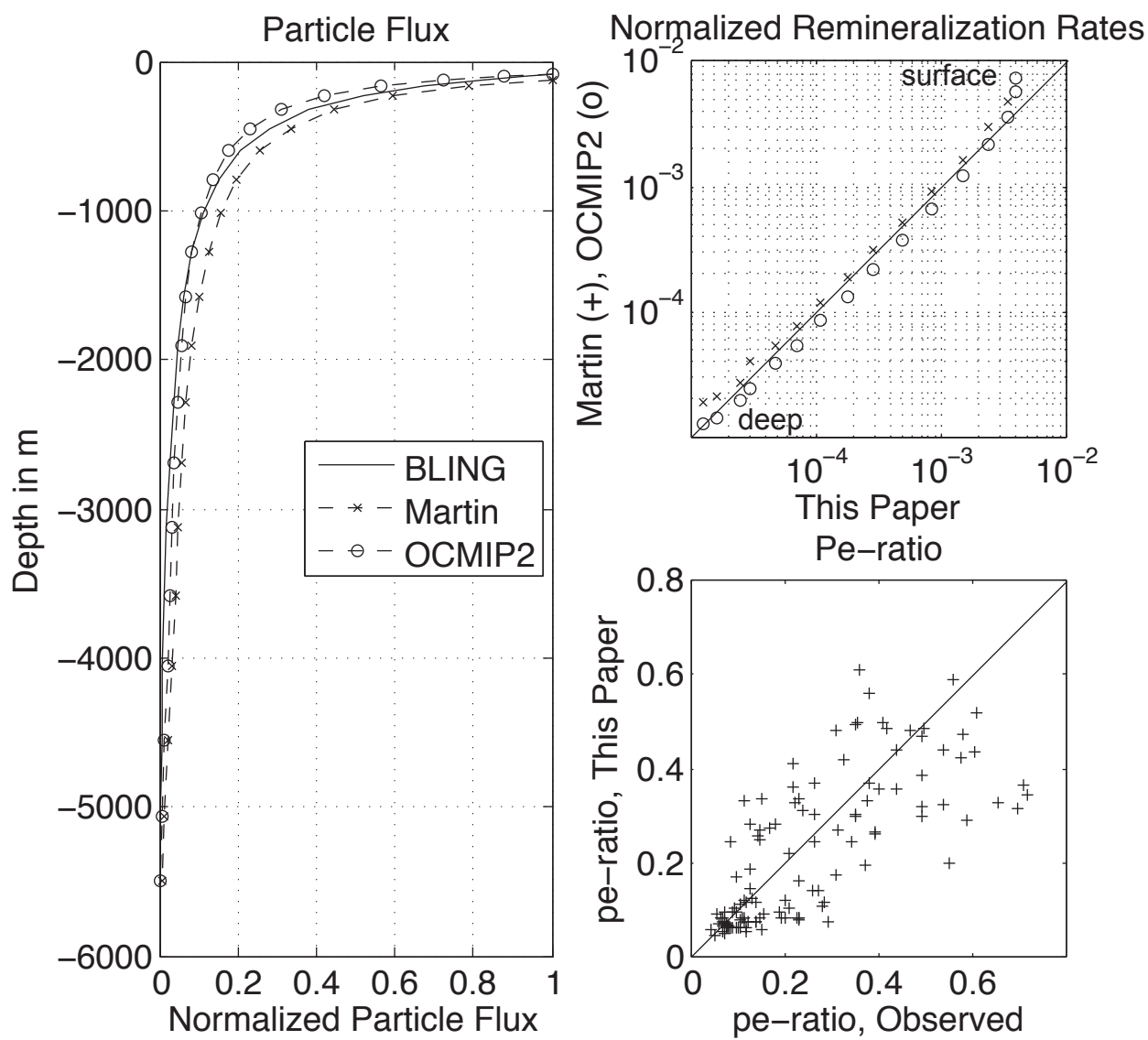
Galbraith et al. Figure 1



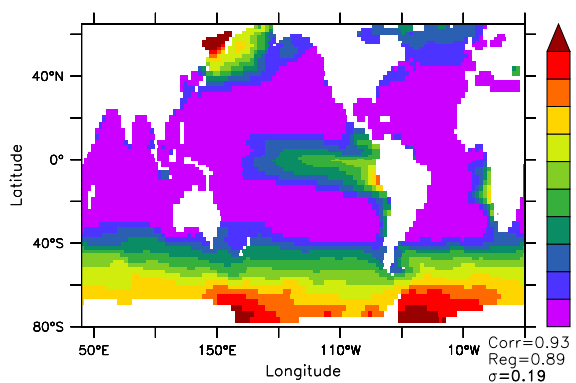
Galbraith et al. Figure 2



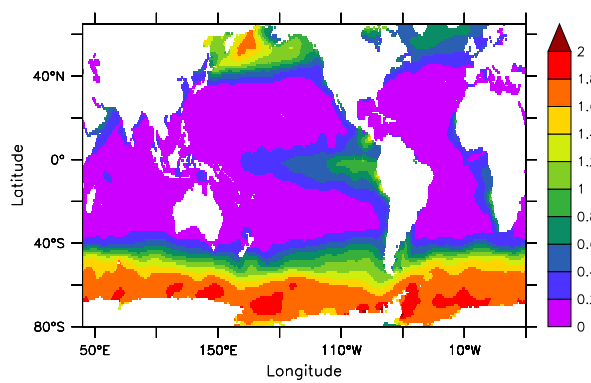
Galbraith et al. Figure 3



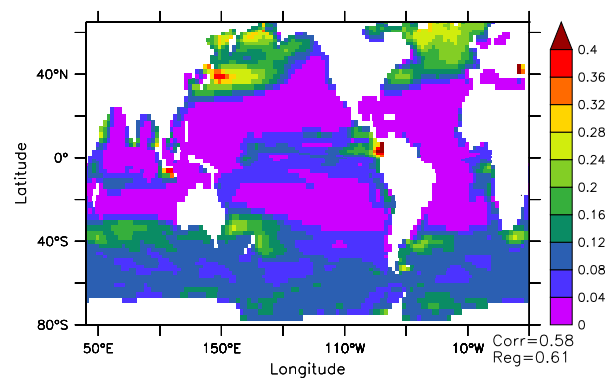
Galbraith et al. Figure 4



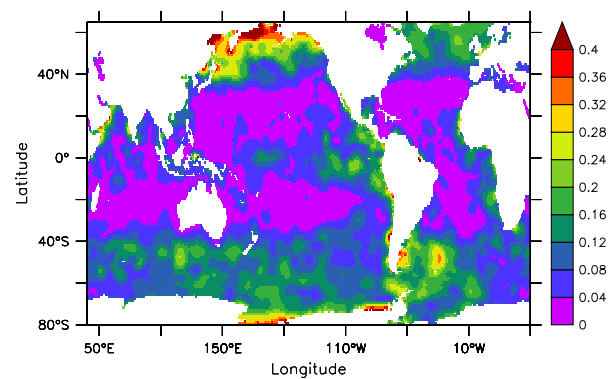
(a) Annual mean PO_4 , model



(b) Annual mean macronutrient, WOA01

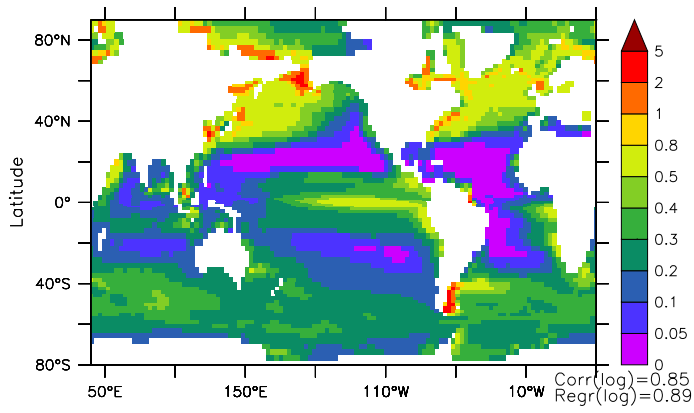


(c) Standard deviation PO_4 , model

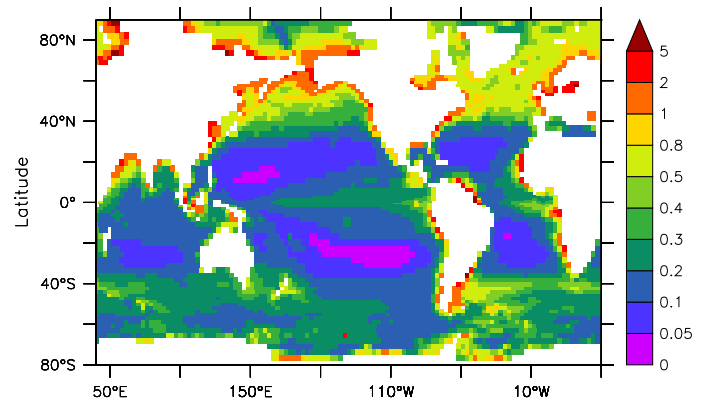


(d) Standard deviation macronutrient, WOA01

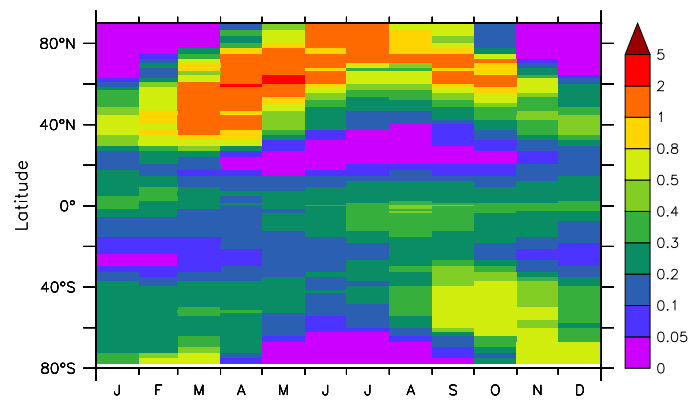
Galbraith et al. Figure 5



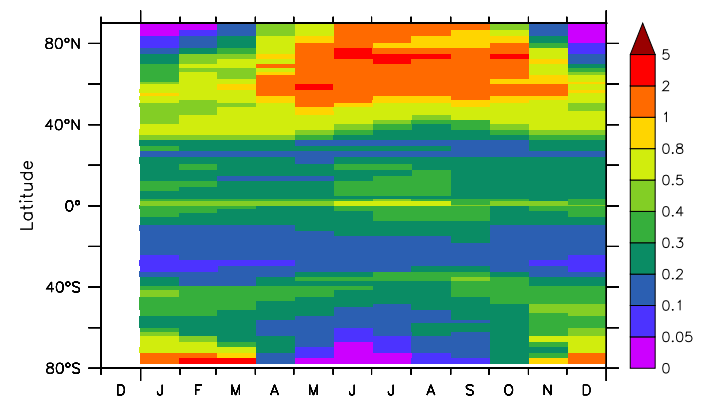
(a) Annual mean chlorophyll, model



(b) Annual mean chlorophyll, SeaWiFS

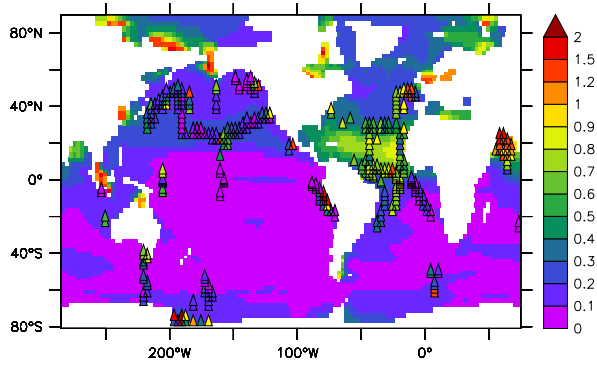


(c) Annual cycle of chlorophyll, model

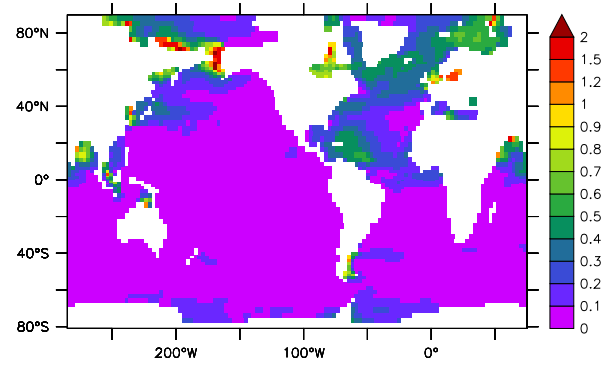


(d) Annual cycle of chlorophyll, SeaWiFS

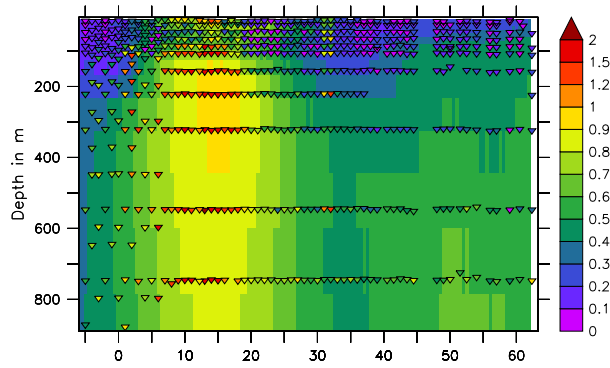
Galbraith et al. Figure 6



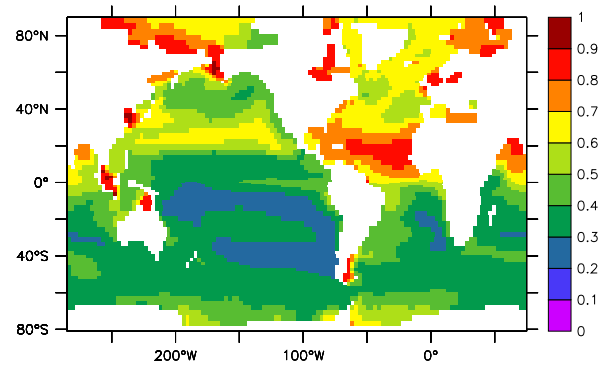
(a) Annual mean surface iron



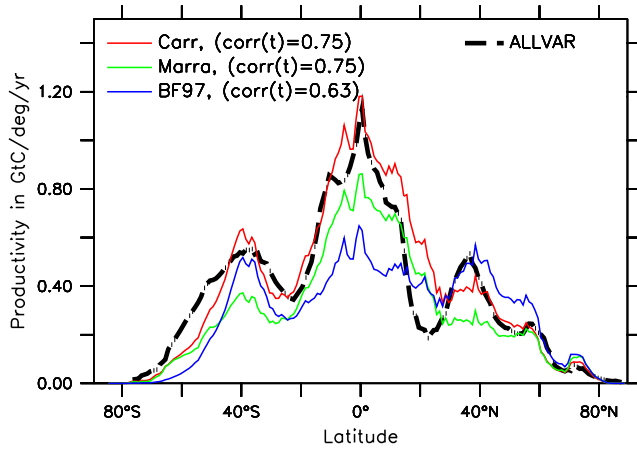
(b) Annual range of surface iron



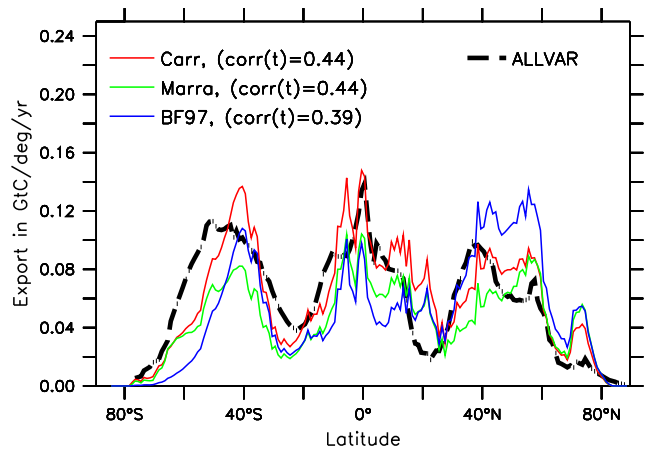
(c) Dissolved iron on A16N section



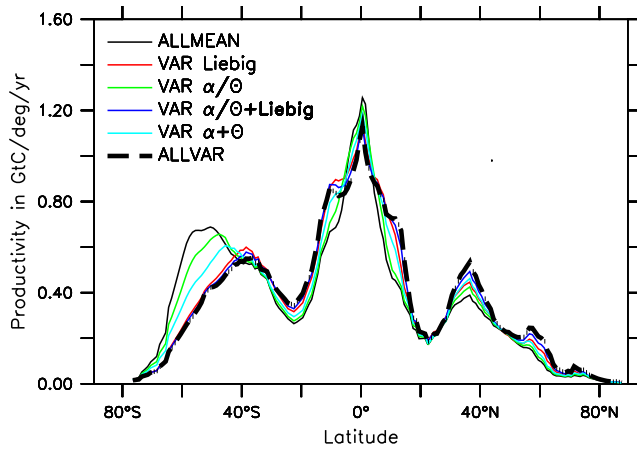
(d) Annual mean surface iron deficiency



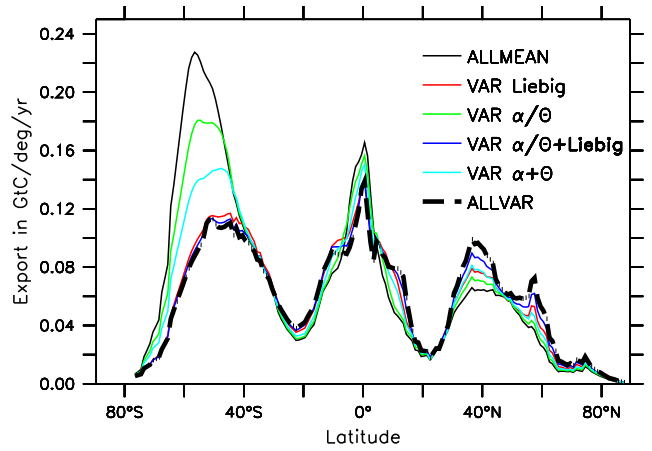
(a) Primary production vs. satellite



(b) Export production vs. satellite

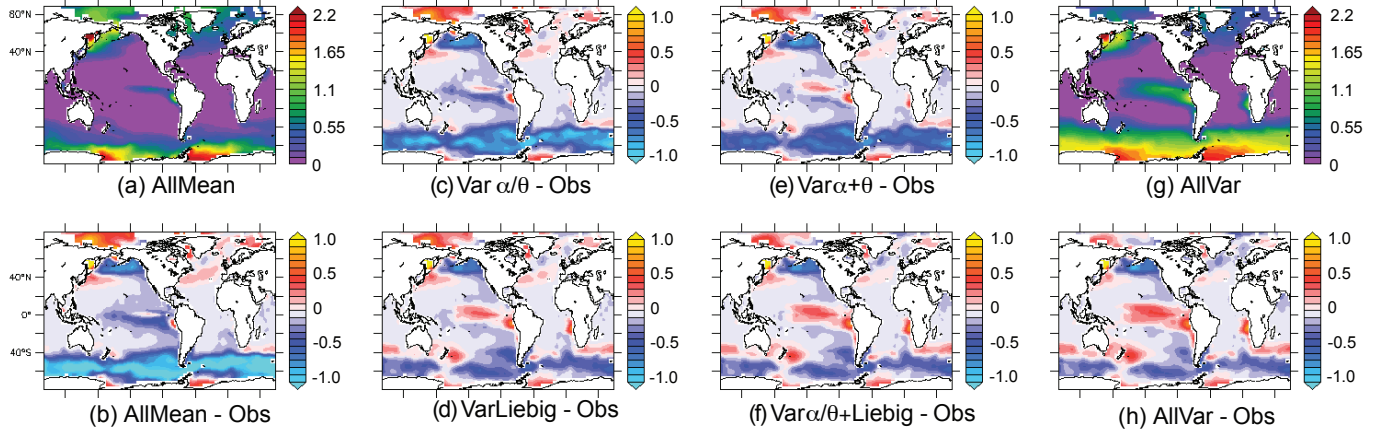


(c) Primary production, experiments

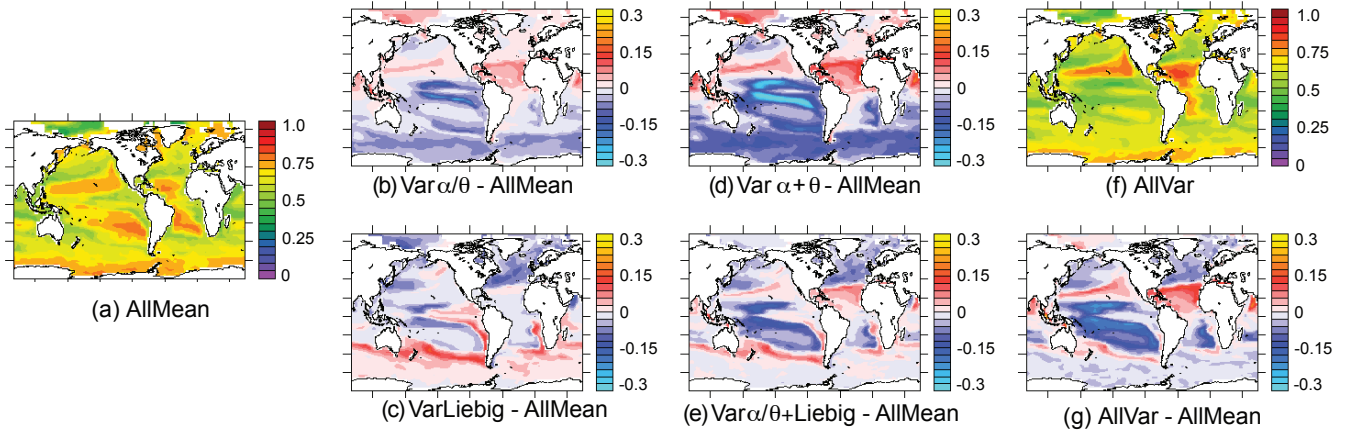


(d) Export production, experiments

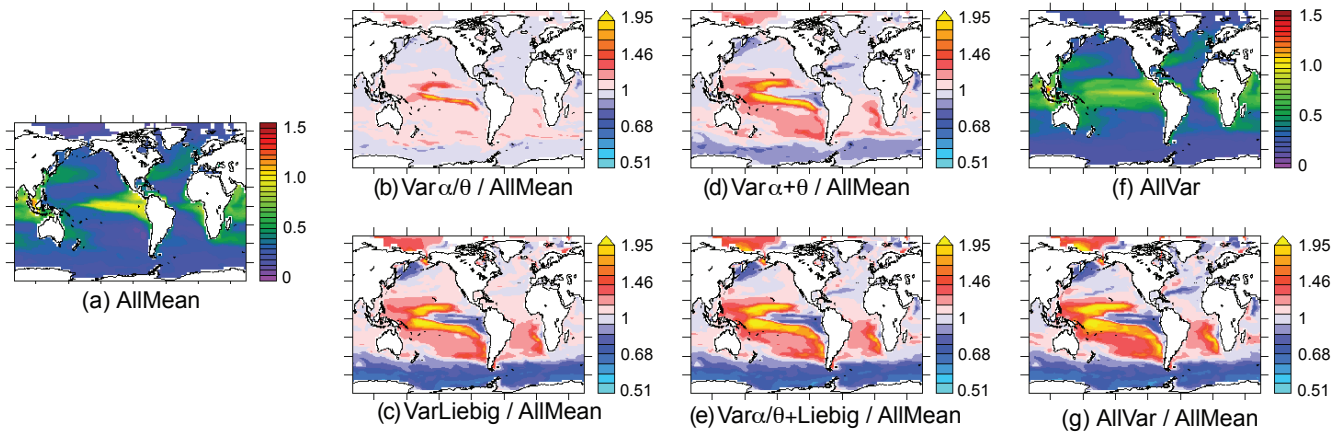
Galbraith et al. Figure 8

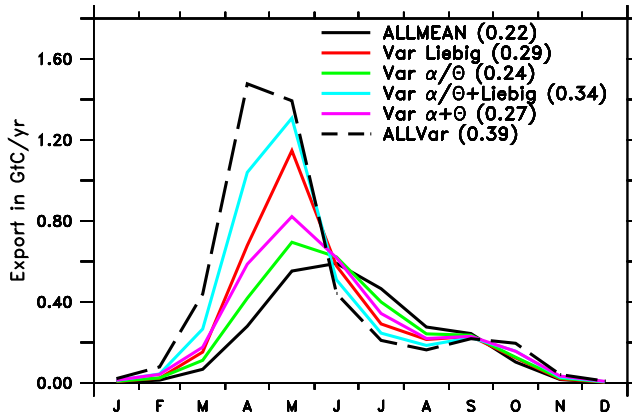


Galbraith et al. Figure 9

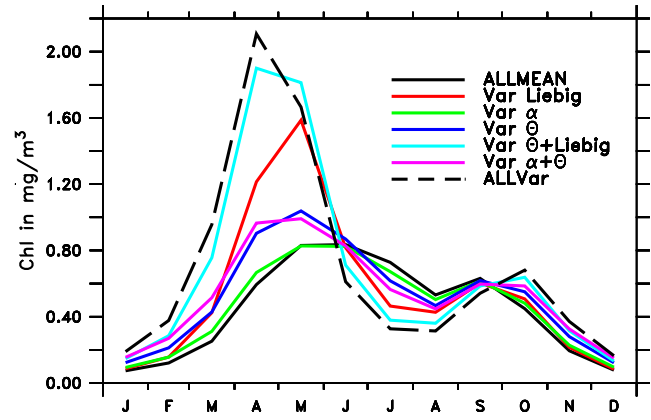


Galbraith et al. Figure 10

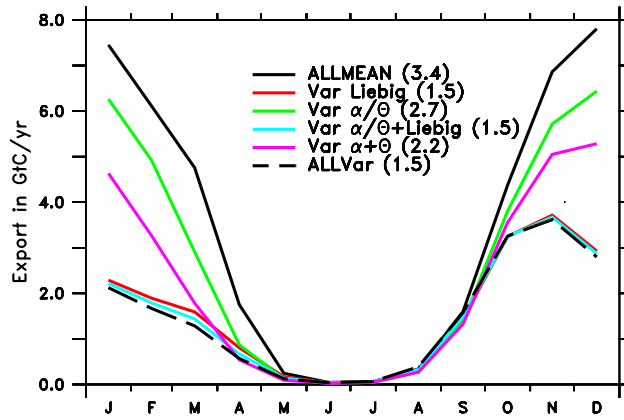




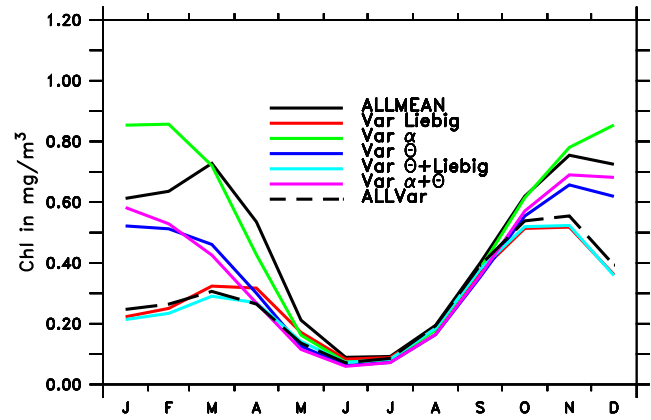
(a) N Atlantic export production



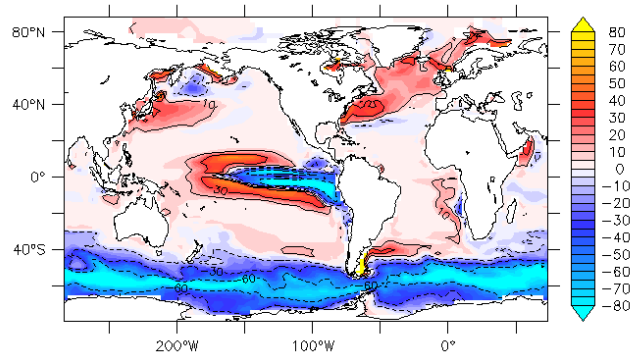
(b) N Atlantic surface chlorophyll



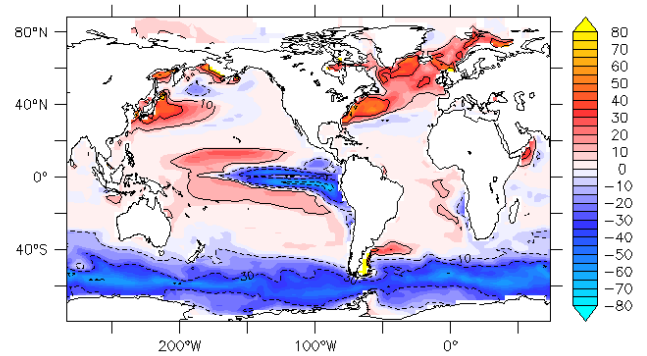
(c) Southern ocean export production



(d) Southern ocean surface chlorophyll



(a) Change in export, linear sum (g C m⁻² a⁻¹)



(b) Change in export, AllVar-AllMean (g C m⁻² a⁻¹)